DISSERTATIONS IN
FORESTRY AND
NATURAL SCIENCES

Sami Väänänen

Functional Imaging of Proximal Femur by Combining Dual Energy X-ray Imaging and Finite Element Simulations

Publications of the University of Eastern Finland
Dissertations in Forestry and Natural Sciences

UNIVERSITY OF
EASTERN FINLAND

SAMI VÄÄNÄNEN

Functional imaging of proximal femur by combining dual energy X-ray imaging and finite element simulations

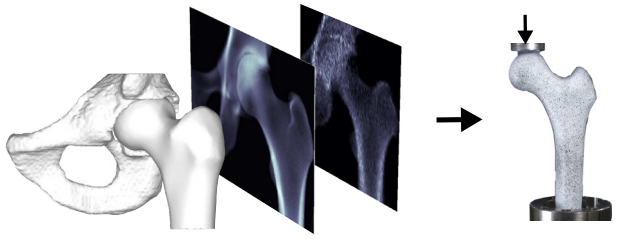

Publications of the University of Eastern Finland
Dissertations in Forestry and Natural Sciences
No 147

Academic Dissertation
To be presented by permission of the Faculty of Science and Forestry for public examination in the Auditorium SN201 in Snellmania Building at the University of Eastern Finland, Kuopio, on September, 20, 2014,
at 14 o'clock.

Department of Applied Physics

Grano Oy
Kuopio, 2014
Editor: Prof. Pertti Pasanen
Prof. Kai-Erik Peiponen, Prof. Pekka Kilpeläinen, Prof. Matti Vornanen

Distribution:
University of Eastern Finland Library / Sales of publications
julkaisumyynti@uef.fi
http://www.uef.fi/kirjasto

ISBN: 978-952-61-1536-8 (printed)
ISSNL: 1798-5668
ISSN: 1798-5668
ISBN: 978-952-61-1537-5 (pdf)
ISSNL: 1798-5668
ISSN: 1798-5668

Author's address:
University of Eastern Finland
Department of Applied Physics
PO Box 1627
70211 Kuopio
Finland
email: sami.vaananen@uef.fi

Supervisors:
Dean Jukka Jurvelin, Ph.D.
University of Eastern Finland
Department of Applied Physics
PO Box 1627
70211 Kuopio
Finland
email: jukka.jurvelin@uef.fi

Associate Professor Hanna Isaksson, Ph.D.
Lund University
Department of Biomedical Engineering,
and Department of Orthopedics
PO Box 118
22100 Lund
Sweden
email: hanna.isaksson@bme.lth.se

Reviewers:
Professor Mark Taylor, Ph.D.
Flinders University
School of Computer Science, Engineering and Mathematics
GPO Box 2100
Adelaide 5001
South Australia
email: mark.taylor@flinders.edu.au

Associate Professor Esther Tanck, Ph.D.
Radboud University Medical Center
Orthopaedic Research Laboratory
PO Box 9101
6500 HB Nijmegen
The Netherlands
email: esther.tanck@radboudumc.nl

Opponent:
Professor Philippe Zysset, Ph.D.
University of Bern
Institute of Surgical Technology and Biomechanics
Stauffacherstrasse 78
3014 Bern
Switzerland
email: philippe.zysset@istb.unibe.ch

ABSTRACT

It is estimated that over 200 million people worldwide have osteoporosis. At present, osteoporosis is diagnosed by measuring bone mineral density (BMD) from the femoral neck or the lumbar spine with Dual-Energy X-Ray Absorptiometry (DXA). However, BMD measured with DXA is only a moderate predictor of fracture risk. It does not take into account any other factors than BMD which could affect the bone quality such as bone geometry or architecture.

This thesis develops and describes methods to reconstruct the 3D shape and internal density distribution of the proximal femur from a single 2D DXA image. Subsequently, a numerical mechanical model is created using the reconstructed shape. The model enables an estimation of the mechanical characteristics and strength of the femur. The strength information accounts for both BMD and geometrical aspects of the femur, and therefore it has a high potential to improve the prediction of the fracture risk. Two of the developed reconstruction methods were based on an average femoral template and feature-based registration between the template and DXA image. The third developed method was based on a statistical shape and density template and intensity-based registration. Feature-based reconstruction techniques were faster whereas intensity-based reconstruction enabled a fully automatic procedure that produced the input for the mechanical simulation. The feature- and intensity-based methods displayed rather similar accuracies. The femoral surface was reconstructed with mean accuracy of one millimeter.

A method which estimates the 3D orientation of a proximal femur in a 2D radiograph was developed. The orientation was estimated with three times higher accuracy compared with that of a trained naked human eye. Thus, the method may be able to differentiate the amount of rotations between two different image sets or to correct the misalignment of the femur in DXA images during feature-based 2D-to-3D reconstruction.

Numerical models need to be validated. Therefore, the surface strains of composite femurs were measured with digital image correlation (DIC) technique during a mechanical compression test. DIC optically traces the displacements and deformations on the surface of the object under loading. The DIC data could reveal,

differentiate and explain sample-to-sample differences between the composite femurs. The surface strains measured with DIC data provides around 50000 spatial measurement points at each time point and therefore generates substantial data for validation of mechanical models.

All of the methods developed and evaluated in this thesis may significantly contribute to development of improved diagnostics methods for osteoporosis in the future.

National Library of Medicine Classification: QT 34.5, QT 36, WE 103, WE 250, WN 200
Medical Subject Headings: Bone and Bones; Bone Density; Femur; Hip Fractures; Osteoporotic Fractures; Osteoporosis/diagnosis; Biomechanical Phenomena; Absorptiometry, Photon; Tomography, X-Ray Computed; Image Processing, Computer-Assisted; Numerical Analysis, Computer-Assisted; Finite Element Analysis; Computer Simulation

Yleinen suomalainen asiasanasto: luu; luuntiheys; reisiluu; osteoporoosi - - diagnoosi; röntgentutkimus; fotoniabsorptiotekniikka; tietokonetomografia; biomekaniikka; simulointi; numeeriset menetelmät

To my dearest
Tiina and Onni

Acknowledgments

This study was carried out during the years 2009–2014 in the Department of Applied Physics at the University of Eastern Finland.

First of all, I would like to thank my supervisors for their guidance during the thesis work and for sharing their expertise. I am deeply grateful to my supervisor Associate Professor Hanna Isaksson for her patient, humane mentoring in the world of science both at work and during conferences, and her help in solving any tricky question. I want to thank my supervisor Professor Jukka Jurvelin for giving me opportunity to work in his professional research group, for all the invaluable help and constantly reminding me of the big picture, and his patient understanding and support each time when I wanted to add one more part to the methods. You both are great role models for future innovative scientists and supervisors.

I would like to thank the official reviewers of this thesis, Professor Mark Taylor, PhD, and Associate Professor Esther Tanck, PhD, for their constructive criticism and for sharing their expertise to improve this thesis.

I am grateful to Ewen MacDonald, D.Pharm., for revising the language of this thesis and Gerard G Netto, PhD, for linguistic guidance during my writing process.

I acknowledge my other co-authors, Adjunct Professor Petro Julkunen, PhD, Adjunct Professor Joonas Sirola, MD, PhD, Professor Heikki Kröger, MD, PhD, Jan Hendrik Waarsing, PhD, Associate Professor Amir Abbas Zadpoor, PhD, Professor Harrie Weinans, PhD, Saber Amin Yavari, PhD, Lorenzo Grassi, MSc, and Associate Professor Gunnar Flivik, MD, PhD, for their contributions in sample collection, and during model constructions, measurements and the preparation of the manuscripts. Especially, I would like to thank Professor Harrie Weinans and his research group who warmly welcomed and hosted me during my research exchange period in Rotterdam and who were so warm and friendly both during and outside working hours. I also want to acknowledge Associate Professor Amir Abbas Zadpoor and his group who invited me to Delft,

shared their profession and helped me through the experimental testing of composite femurs. Lorenzo Grassi, you are a cheerful fellow who has always time to help irrespective of which side of world you are located. It is pleasure to work with you.

I want to thank the whole Biophysics of Bone and Cartilage group. It has been a privilege to work with such a devoted and smart persons. Especially, I want to thank Mikko Nissi for guiding me into the world of Linux and for giving me precious help at the beginning, and also to the others who have shared a room with me during these years. We have left no issue between earth and heaven undiscussed. I also want to thank the most caring and helping colleague Markus Malo who has gone the studies through the same pace all these years and who also is delighted to share the joy of dissertation defense with me on the same day.

I would like to thank the staff of the Department of the Applied Physics for their efforts and help during this thesis project.

This thesis was financially supported by the Finnish Cultural Foundation's North Savo regional funding, Instrufoundation, Academy of Finland (128863, 14088), Strategic Funding of University of Eastern Finland (929711), Department of Clinical Physiology and Nuclear Medicine of Kuopio University Hospital (EVO grants 2009/00117, 2010/00013, 2011/00108), Foundation for Advanced Technology of Eastern Finland, Swedish Research Council (2011-5064), Crafoord foundation, and Natinal Graduate School of Musculoskeletal Disorted and Biomaterials. I want to also acknowledge CSC - the Finnish IT Center for Science for computational tools and resources.

Finally, I would like to thank my friends who have supported me during my work and moved my thoughts away from work. I am deeply grateful to my parents Outi and Seppo Väänänen who have supported me through my entire life. I want to express my love-filling thanks to my dearest Tiina for her continuous support, love and understanding during this project, and our darling son Onni who always brings joy into our life. Their presence made this thesis possible.

Kuopio, 5th of August 2014

Sami Väänänen

ABBREVIATIONS

ANN	Artificial Neural Networks
AUC	Area Under ROC Curve
BMC	Bone Mineral Content
BMD	Bone Mineral Density
BMU	Bone Multicellular Unit
DIC	Digital Image Correlation
DICOM	Digital Imaging and Communications in Medicine
DRR	Digitally Reconstructed Radiograph
DXA	Dual-Energy Xray Absorptiometry
GA	Genetic Algorithm
GPA	Generalized Procrustes Analysis
HU	Hounsfield Unit
MAC	Modal Assurance Criterion
MLP	Multilayer Perceptor
PCA	Principal Component Analysis
QCT	Quantitative Computed Tomography
ROC	Receiver Operator Characteristics
SAD	Sum of Absolute Difference
SAM	Statistical Appearance Model
SD	Standard Deviation
SSM	Statistical Shape Model
SVD	Singular Value Decomposition
TPS	Thin-Plate Spline
$CTDI_{vol}$	Volumetric CT Dose Index
WHO	World Health Organization

SYMBOLS AND NOTATIONS

α	Attenuation coefficient
M	Areal mass
K	Bulk modulus
ϕ	Displacement vector
p	Dimension of the problem
c_{ijkl}	Elastic coefficient
I	Intensity
μ	Linear attenuation coefficient
P	Landmark
$\theta_{\min}$	Minimum solid angle
Ω	Calculation region of cost function
ν	Poisson's ratio
G	Shear modulus
ϵ	Strain
$\mathbf{C}$	Stiffness matrix
σ	Stress
U	Solution of biharmonic equation
^{T}	Matrix transpose
ϵ_v	von Mises strain
w	Weights in ANN
E	Young's modulus

LIST OF PUBLICATIONS

This thesis consists of the present review of the author's work in the field of medical physics. The following selection of the author's publications is referred to by the Roman numerals:

I S. P. Väänänen, H. Isaksson, P. Julkunen, J. Sirola, H. Kröger, and J. S. Jurvelin, "Assessment of the 3-D shape and mechanics of the proximal femur using a shape template and a bone mineral density image," *Biomechanics and modeling in mechanobiology,* **10,** 529–538 (2011).

II S. P. Väänänen, J. S. Jurvelin and H. Isaksson, "Estimation of 3D shape, internal density and mechanics of proximal femur by combining bone mineral density images with shape and density templates," *Biomechanics and modeling in mechanobiology,* **11,** 791–800 (2012).

III S. P. Väänänen, H. Isaksson, J. H. Waarsing, A. A. Zadpoor, J. S. Jurvelin, and H. Weinans, "Estimation of 3D rotation of femur in 2D hip radiographs," *Journal of Biomechanics,* **45,** 2279–2283 (2012).

IV S. P. Väänänen, S. Amin Yavari, H. Weinans, A. A. Zadpoor, J. S. Jurvelin, and H. Isaksson, "Repeatability of digital image correlation for measurement of surface strains in composite long bones," *Journal of Biomechanics,* **46,** 1928–1932 (2013).

V S. P. Väänänen, L. Grassi, G. Flivik, J. S. Jurvelin and H. Isaksson, "Automatically generated 3D shape, density and finite element mesh of proximal femur from a DXA image," *submitted for publication,* (2014).

 This thesis also contains previously unpublished data.

AUTHOR'S CONTRIBUTION

This thesis is based on five research articles on osteoporosis diagnostics, bone biomechanics and medical image analysis. The idea of combining DXA imaging, 3D reconstruction and mechanical simulation originated from the author's supervisors. The author has contributed to the study design, and carried out the development of the presented methods, simulations, analyses and measurements, with the exception of most of the CT and DXA image acquisitions. The author was the main writer of all studies.

Contents

1 Introduction

The primary responsibility of the skeleton is to bear loads. Its other functions include protection and support of the internal organs, blood production and mineral reserving. In order to maintain its endurance, optimal strength and lightness throughout life, bone continuously undergoes remodeling [1–4]. Normal activity results in microscopic fractures in the bone which are dissolved and replaced by new intact bone [1]. Bone also responds to external forces by increasing its mass when the loads increase and by decreasing its mass when the forces are reduced [1]. However, due to aging or some symptoms, the balance between the bone resorption and formation may be disturbed. This can lead to reduced bone mass and strength [5].

Osteoporosis is defined as a disease where skeletal strength is impaired and the fracture risk is increased [5–7]. Osteoporotic fracture affects loss of mobility and self-determination and therefore leads to a major loss of quality of life [8]. It has been estimated that over 200 million people worldwide have osteoporosis [9, 10]. Hence, it is the most common metabolic bone disease. In the European Union, about 30 % of all women over 50 are affected by osteoporosis [11]. In 2000, the number of osteoporotic fractures in the European Union was estimated to have been 3.1-3.7 million [12,13]. This resulted in direct costs of €32 billion to the health care services [10,13]. Furthermore, the progressively aging population, especially in the developed countries, leads to an increase in osteoporosis prevalence [14, 15], and it is estimated that in 2050 the cost of osteoporotic fractures in Europe will rise to €76.8 billion [13]. Hence, effective diagnostics, prevention and treatment will be essential in the successful osteoporosis management.

Current osteoporosis diagnostics is largely based on measurements of bone mineral density (BMD), using dual energy X-ray absorptiometry (DXA) of the hip or the lumbar spine [5, 16]. The BMD value is compared with the mean value of the healthy young population in the region, and the result is converted to a T-score value [5, 10], which forms the basis of the individual's fracture

risk. Paradoxically, although DXA-based BMD is a good measure of bone density, it is only a moderate predictor of fracture risk [17,18]. It has been demonstrated that only 30 % of all low-energy fractures can be explained by changes in BMD alone [19]. This indicates that better methods, including different types of information in addition to BMD, are needed for prediction. Bone quality includes all characteristics that increase the bone's resistance to fracture, including BMD, bone architecture, geometry, turnover and mineralization [20–22].

One way to assess resistance of bone to fracture is to estimate the ultimate strength of bone. Usually this is done with finite element (FE) modeling, where the geometry is based on 3D images of the femur obtained from clinical quantitative CT (QCT) devices [23–33]. It has been shown that FE analysis of the bone can explain at least 20 % more of the variance in femur strength than DXA alone [29]. However, QCT imaging is expensive and depending on the imaging settings, it may result in about 300 times larger radiation doses than DXA imaging [34]. Therefore, there is a clear need to develop a method that could assess bone strength accurately without 3D CT images.

Since the DXA images are two-dimensional, they lack information on the direction of tissue depth. Consequently, it is not possible to develop a 3D femur model using DXA alone. Templates which include information of general femur shapes, density distribution and their variation in population in all three dimensions could be helpful. Earlier, the femoral shape has been reconstructed using prior information from CT images and one or several 2D radiographic images [35–39]. However, many of these methods require more than one radiological image [35, 37], and they are not based on the DXA image [36, 40]. There is still no method that would automatically reconstruct both femoral shape and internal density from a single DXA image and combines it with FE modeling that can automatically calculate the strength of the femur.

The aim of this thesis is to improve methods for assessing bone strength and fracture risk, based on a combination of DXA images and FE modeling. This thesis also introduces the digital image correlation method [41], which can be used to evaluate strains at the bone surface during loading of the proximal femur. This strain data

can be used to validate FE simulations. The underlying hypothesis of this study is that 3D geometry and the inner architecture of the femur can be estimated from 2D DXA images. A further hypothesis is that the result of strength analysis correlates with the true strength of the femur. The final hypothesis is that the analyzed strength and strain of the femur are highly related to an individual's fracture risk. Therefore, the developed method must be capable of assessing the maximum load that the femur can withstand before fracture.

2 Bone

Bone is a optimized composite material that has high stiffness and strength combined with the lightness of wood [1]. Due to its high strength, bone is able to resist heavy compressive loads, tensions and torsions, whereas its light weight enables quick sprints and leaps [21,42]. Since bone is a living material, it can constantly modify its strength and weight by varying its shape, structure and composition. Thereby, bone optimally adapts to the existing mechanical environment [1, 43]. These natural processes are called bone formation, modeling and remodeling [1]. If bone fails under a high impact load, for example in a car accident or when slipping on ice, it almost instantly begins a repair process in order to restore its weight-bearing ability [1].

2.1 BONE COMPOSITION

Bone is a composite material constructed mainly of mineral and collagen. The collagen represents an organic matrix which is stiffened by crystals of calcium and phosphate-based mineral hydroxyapatite [20]. The organic matrix is responsible for the tensile and shear strengths of bone whereas the mineral matrix carries the compressive loads [1]. Together, organic and mineralized matrices form stiff composite material with high endurance against both tensile and compressive forces. An increase in the mineral density increases the stiffness of bone but sacrifices its ductility [20]. In human bone, around 60 % is mineral [20], 30 % is organic matrix, and the rest is mainly blood vessels, cells and water [1].

2.2 BONE BIOLOGY AND REMODELING

Bone has three main cell types: osteoclasts, osteoblasts and osteocytes. Osteoclasts resorb or dissolve bone. The osteoblast family consists of osteoblasts that form bone, but also of the osteocytes that help to maintain bone, and bone lining cells that cover the bone surface (Figure 2.1) [1].

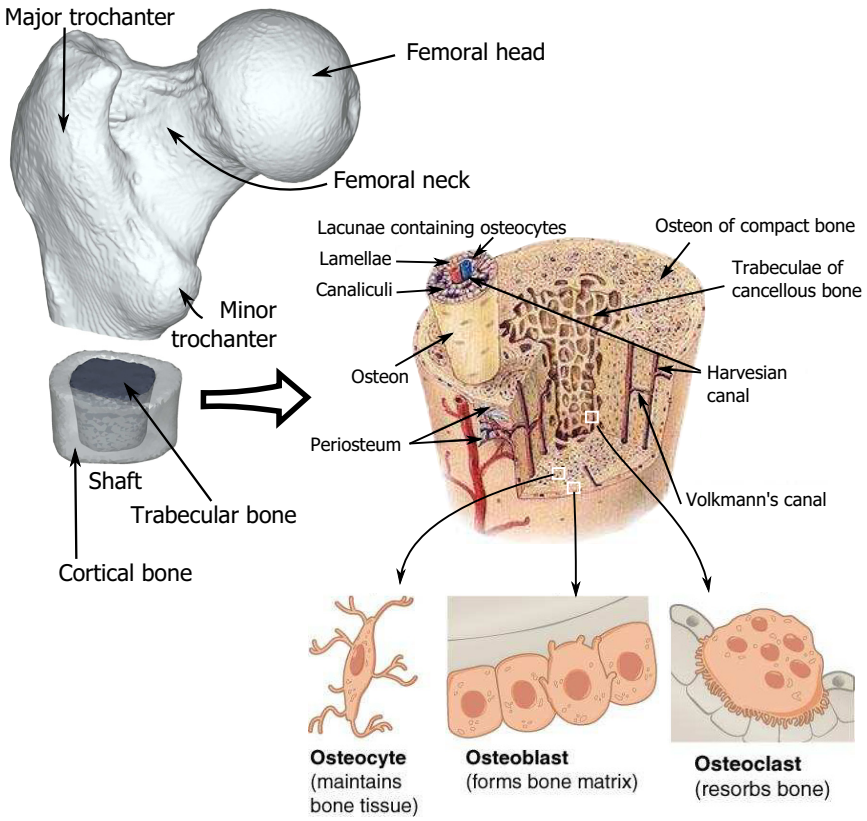

Figure 2.1: Parts of proximal femur, structure of bone and bone cells. Part of the image is a modified version from [44] according to Creative Commons Attribution 3.0 Unported license [45]

Osteoclasts are large cells with many nuclei. The human osteoclasts have a diameter of 15 to 20 μm [1]. Osteoclasts originate from the macrophage lineage, which are types of blood cells that are dedicated to dissolving bacteria, harmful foreign particles or other cells or tissue [46]. Osteoclast precursors are monocytes which are formed in the red bone marrow and then released to the blood circulation [47]. Osteoclasts resorb underlying bone by releasing hydrogen ions and several hydrolytic enzymes which dissolve the mineral and organic components of the bone matrix [46]. After completion of this process, they deactivate themselves or undergo apoptosis based on which regulation signals they receive from other cells [20]. Osteoclasts are regulated by several hormones, including the parathyroid hormone (PTH) and calcitonin [48]. Osteoclasts and osteoblasts also regulate themselves since osteoclast activity is also mediated by the interaction of the molecules osteoprotegerin and RANK ligand which are produced by osteoblasts [49]. These molecules also regulate osteoclast differentiation [49].

Osteoblasts are cells with a single nucleus. They originate from the mesenchymal stem cells, which are precursors of different connective tissues [48]. Mesenchymal stem cells are located at the periosteum and bone marrow, and they can differentiate into many other celltypes, *e.g.*, osteoblasts, cartilage cells and fat cells [48]. Osteoblasts are located at the bone surface, where they synthesize new bone. Since individual osteoblasts cannot create new bone themselves, they function together and organize themselves into bone forming units or bone multicellular units (BMUs) called osteons [20]. When osteoblasts create new bone, they synthesize collagen and other proteins, which form the organic matrix of bone [1]. Then hydroxyapatite and a small amount of other minerals together form the mineralized bone matrix [1]. During bone formation, those osteoblasts that become surrounded by the bone matrix differentiate into osteocytes. Other osteoblasts remain on the surface of the new bone and differentiate into bone lining cells. The rest of the osteoblasts remain as such or undergo apoptosis [48]. Osteoblasts have receptors for vitamin D, estrogen and PTH, and they secrete factors such as RANK-ligand which activates osteoclasts [50].

Osteocytes are bone cells which are surrounded by the bone matrix. With their long branches they connect to other osteocytes

and lining cells [20]. They are believed to be the bone sensing cells, *i.e.*, one of their properties is to sense strains inside bone. They secrete growth factors which activate lining cells or stimulate the osteoblasts [20]. It is believed that they are able to direct both bone remodeling according to strain direction and repair damage due to fatigue [51].

Lining cells cover the whole bone surface. They are differentiated from osteoblasts and are flat-shaped. Lining cells can release calcium from bone by activating osteoclasts if the calcium concentration is too low in blood. They also protect bone from dissolving chemicals and detect hormones which initiate bone remodeling [1, 20, 48].

2.3 BONE STRUCTURE

Based on their general appearance, bones can be classified into short, flat or long [1]. Short bones, such as vertebral bodies, have about similar lengths in all directions, and their shape varies from cuboidal to irregular. Flat and long bones, such as the femur or scapula, have one or two dimensions that are much longer than the others. Long bones, such as the femur, consist of a tubular diaphysis at the middle and expanded meta- and epiphyses at both ends (Figure 2.1) [1]. Cartilage covers these bone ends so that inside joints there is almost frictionless connection to other bones. The other long bone surfaces, except for the connection points with tendons, ligaments and connection points of joint-enclosing membranes, are covered by a periosteum [1].

The tubular diaphysis and thin surfaces of epiphyses and metaphyses consist of cortical bone, and the rest of the bone tissue is trabecular bone, as shown in Figure 2.1. In the mature human skeleton, around 80 weight percent is cortical bone [1]. Cortex and trabecular bone have a similar matrix composition and nano structure. However, cortical bone is much more dense and has lower porosity (~10 %) [1, 21] than trabecular bone, which consists of interconnected small rod- and plate-like elements. The porosity of human trabecular bone is between 50-90 % [1, 52], and the pores between the rods and plates are filled with bone marrow, similarly as the interior of the diaphysis. Since the surface-to-volume ratio

is higher in trabecular bone than in cortical bone, it undergoes a higher remodeling rate [1]. Therefore, trabecular bone responds to altered mechanical stimuli faster than cortical bone. The spongy structure in trabecular bone may also absorb load energies [20,53].

At the microscopic level, cortical bone consists of cylindrical units called osteons [1,54] (Figure 2.1). At the center of each osteon there is a Harvesian canal which includes blood vessels, lymphatic vessels and occasionally nerves. The canaliculi, which branch radially from the central canal, include the processes of osteocytes [20, 55]. The Harvesian canals connects periosteal and endosteal surfaces [1]. Osteons are distinguished and bounded by cement lines [54], which define the remodeling lines of bone [20].

2.4 BIOMECHANICAL PROPERTIES OF BONE

The bones in our body bear the loads which the body experiences during everyday life [42, 56]. The mechanical properties of bone can be characterized using mechanical tests where bone is compressed, stretched, twisted or indented. These properties may differ depending on the geometrical scale of interest [57]. The result is typically viewed by presenting the forces as a function of the deformations [48, 58]. The data can also be transformed into stresses σ and strains ϵ, which are geometry-free measures (Figure 2.2). The **stress** is defined as the applied force divided by the area of the sample, whereas **strain** is the deformation of the sample divided by its original length [59]. Thus these are material properties rather than structural properties. If the bone is exposed to only a small or moderate stress, it behaves elastically, *i.e.*, it is able to return to its original shape when the load is released. The curve at the elastic region is a straight line, and the coefficient of the slope is called the elastic or **Young's modulus** E, and it represents the intrinsic **stiffness** of the bone. The region where the deformations of the bone are permanent is called the **plastic** region, which is separated from the linear region by the **Yield point**. Bone strength refers to the force or stress where the bone **ultimately fails**, *i.e.*, the stress, where the bone reaches its maximum stress, after which it declines rapidly. **Ductility** describes how much the bone is able to deform at the plastic region before it reaches its ultimate failure. **Toughness**

describes how much work is needed to break the bone, *i.e.*, how much energy it can absorb, and it is calculated as the area under the stress-strain curve.

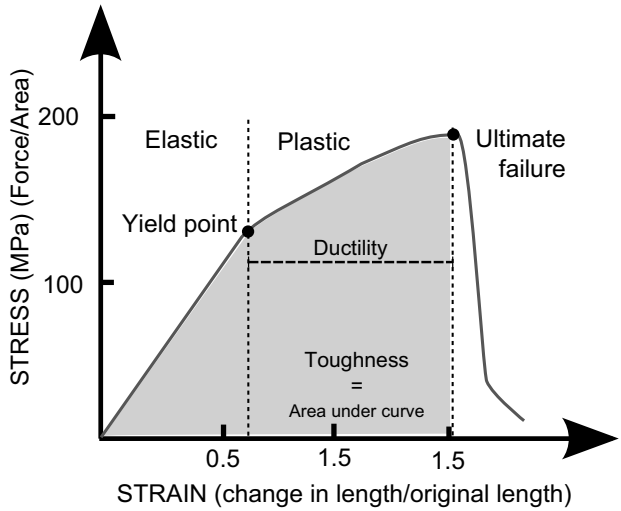

Figure 2.2: The stress-strain curve of bone is divided into elastic region, where bone recovers to its original shape after loading, and plastic region, where deformations are permanent. These two regions are separated by the yield point.

Typical ultimate strengths and Young's moduli of human cortical bone are presented in table 2.1. The ultimate strength and Young's modulus are also dependent on the strain rate. When the strain rate grows from extremely slow to high impact strains (from 0.001 to 1000 1/s) the ultimate tensile strength approximately triples and the Young's modulus doubles [58, 60]. Thus, bone has viscoelastic properties [61,62], but within the range of physiological loading bone viscoelasticity can often be neglected [63, 64].

Table 2.1: Material properties of femoral cortical bone, where σ_C is the ultimate compressive strength, σ_T is the ultimate tensile strength and E is the Young' modulus [58, 65]

	σ_C (MPa)	σ_T (MPa)	E (GPa)
Longitudinal	193	133	17.0
Transverse	133	51	11.5
Shear	68		3.3

The femoral strength is measured by loading the whole bone or part of it until fracture. The loading conditions can mimic those found during the stance phase as the femur is loaded axially [66–70], or a fall on the side when the load direction is lateral [71–74]. In both loading scenarios, the load is directed to the femoral head and the shaft is constrained with a holder. In side-fall loading, also the lateral side of the major trochanter is supported. In experiments, the angle between the diaphysis and load vector typically varies from 0° [75, 76] to 15-25° [29, 69], and the loading rate varies from very low (0.5mm/min [26]) to a physiological loading rate (30mm/s [64]).

2.5 OSTEOPOROSIS

Osteoporosis is defined by the World Health Organization (WHO) as "a systemic skeletal disease characterized by low bone mass and microarchitectural deterioration of bone tissue with a consequent increase in bone fragility and susceptibility to fracture" [77]. Thus, low bone mass is an important factor for increased fracture risk. However, other factors of bone quality, such as geometry, microstructure and bone composition, also contribute to skeletal fragility [6, 7, 20, 78, 79]. Osteoporotic fragility fractures occur most commonly at the wrist, spine and hip [8] of which hip fracture exhibits the highest mortality rate. Among 65 years old women, the mortality rate at 6-months after a hip fracture increases from a baseline of 1.5 % to 7.5 %, and the mortality rate of men increases even more [80].

In osteoporotic bone, the BMU remodeling is out of balance, *i.e.*, more bone is being resorbed by osteoclasts than is formed by osteoblasts [21]. This imbalance may result from increased bone resorption, decreased bone formation or a combination of both processes.

Women above 50 comprise the largest osteoporotic patient population. This is mostly a result of the decline in estrogen levels after menopause, which both increases the imbalance between bone resorption and formation and increases the number of BMUs [21, 81]. Therefore, 80 % of hip fractures occur in women and 90 % of hip fractures occur in individuals older than 50 [81]. Since the

surface-to-volume ratio is higher in trabecular bone than in cortical bone, the imbalanced bone remodeling affects trabecular bone more quickly [20]. Therefore, increased porosity and decreased number of trabeculae per volume unit are more prevalent at an early stage of osteoporosis than changes in the cortical bone [1, 20]. Most of the osteoporotic fractures occur in regions with high amounts of trabecular bone and a thin cortical shell, such as at the epiphysis of the wrist, the femoral neck or the spine [82].

2.5.1 Risk factors and prediction of fracture

More than 80 risk factors for osteoporosis have been recognized [83,84]. These can be divided into risk factors related to bone mass, clinical risk factors, geometrical risk factors and microarchitectural risk factors. Many of these can be used for fracture prediction.

Osteoporosis results in a lower bone mass. The current golden standard to diagnose osteoporosis and to predict fractures is to measure the areal BMD at the femoral neck or lumbar spine with DXA imaging (see section 3.2) [7,13,16,85–87]. The measured BMD is compared to healthy subjects and a T or Z score is calculated [16]. In the T score, the patient's BMD is compared to that of healthy young adult females and in the Z score, the patient's BMD is compared to the BMD of persons of the same age and gender [5]. The following thresholds are used to diagnose osteoporosis [5,16]:

1. Normal: BMD is above -1 standard deviation (SD) of the average adult healthy young females. (T-Score $\geq$ -1)
2. Low bone mass (osteopenia): BMD is between minus one and minus 2.5 SD of young healthy adult females (-1 > T-score $\geq$ -2.5)
3. Osteoporosis: BMD is below 2.5 SD of the reference mean of young adult females. (T-score < -2.5)
4. Severe or established osteoporosis: BMD is below 2.5 SD of the mean of reference standard of young adult females and the patient has a history of at least one fragility fracture.

When the BMD at the femoral neck decreases by one SD, the hip fracture risk increases 2.6-fold [16]. In addition, an accelerated

rate of BMD loss increases the fracture risk. If the loss in BMD at the femoral neck in men is over -0.034 g/cm2 in 4.6 years, the fracture risk is 6.3-fold compared to men who maintained their BMD over time [88]. The ability of BMD to predict fractures is generally the same as the ability of blood cholesterol to predict heart diseases or the ability of blood pressure to predict the risk of stroke [81, 89]. However, BMD alone is only a moderate predictor of fractures. Trochanteric femoral fractures are better associated with low BMD whereas, *e.g.*, for cervical fractures the femoral geometry seems to play a significant role [90]. BMD explains around half of the bone strength [91, 92]. More than half of the patients with fragility fractures are classified as being osteopenic, not osteoporotic [19, 93]. BMD's ability to discriminate between fracture and non-fracture groups is moderate. The discrimination ability is usually indicated with the area under the receiver operator characteristic (ROC) curve (AUC) , and BMD has typically a value between 0.6-0.75 [84]). Therefore, DXA alone is not sufficient to determine which individual will experience a fragility fracture. Thus, the predictive ability of DXA alone is not cost-effective enough to recommend its use in population screening studies [89].

Several clinical risk factors have been identified for fragility fractures that are independent of BMD including history of fracture, demographic and physical characteristics, use of other medication such as glucocorticoids, family history of fracture, cigarette smoking, ample alcohol consumption, and low bodyweight [81, 84]. Age is the most significant risk factor, even greater than BMD. Within women aged 55-85, the impact of age on the fracture risk is 11 times higher than the impact of BMD [94]. With respect to the other risk factors, parental hip fracture and use of glucocorticoids are strong predictors, whereas smoking and alcohol consumption are milder risk factors for fragility fractures [84]. Physical condition and muscle strength are associated with fracture probability since they affect the individual's probability to fall [95, 96].

FRAX is a fracture risk assessment tool developed by WHO [97]. In FRAX, the clinical risk factors, with or without BMD, are combined to form a multivariate Poisson regression model. This returns a 10-year prediction for the fracture risk. FRAX's ability to discriminate between people with or without fragility fracture in the future

varies depending on whether BMD is included in the regression model. When BMD is not used in the model, the AUC is around 0.65, and it increases up to 0.75 when the BMD is included [98]. When BMD is not included in FRAX, it is less able to discriminate hip fractures than BMD alone, but the discrimination ability increases slightly over that of BMD alone when the BMD is included into the FRAX model [98].

The geometry of the proximal femur has been shown to play a significant role in fracture risk [99], especially in cervical osteoporotic fractures [90]. Different geometrical parameters, such as the thickness of the femoral neck and shaft cortices, and especially the femoral neck-shaft angle and hip axis length, can discriminate fracture and control groups [90, 100, 101]. Interestingly, a large neck-shaft angle is associated with both increased fracture risk and a more urban lifestyle [99, 102]. The structure of bone has also been shown to correlate with bone strength and fracture risk [103–106]. However, most of the current fracture risk prediction tools, such as FRAX, do not take account of hip geometry. Usually, geometrical parameters have to be measured manually, which makes them less suitable for clinical use.

2.5.2 Treatment of osteoporosis

The consequences of osteoporosis can be managed with lifestyle modifications, which include maintenance of mobility and stability in order to prevent falls, the cessation of smoking and reduction of alcohol consumption, and prevention of deficiency of nutrition. Especially, an appropriate amount of vitamin D and calcium intake are recommended for every patient with osteoporosis [8, 107].

Osteoporosis treatment can be divided into antiresorptive drugs and anabolic drugs. Bisphosphonates, such as alendronate, risedronate and zoledronate, reduce the number of BMUs and amount of resorption of bone at each BMU by guiding osteoclasts to apoptosis [107]. Raloxifene inhibits bone resorption by having estrogenic actions on bone [81]. Denosumab inhibits RANK ligand which is one of the primary signals for bone resoption [8]. Anabolic drugs, such as the parathyroid hormone, induce the activity of osteoblasts and therefore bone formation [8].

3 Radiographic methods for prediction of fragility fractures

3.1 X-RAY ABSORPTIOMETRY

Wilhelm Röntgen discovered X-rays and their ability to pass materials opaque to visible light in 1895 [108,109]. A few weeks after the discovery, X-rays were used for medical imaging for the first time when he imaged his wife's hand [108].

In modern native X-ray imaging, an X-ray tube emits radiation which is directed through the patient. The portion of attenuated radiation at each location is measured with an X-ray film or a digital detector. When radiation interacts with atoms in the penetrated matter, the x-rays attenuate as

$$I(x) = I_0 e^{-\mu x} \tag{3.1}$$

where I is the intensity at location x, I_0 is the initial intensity and μ is the linear attenuation coefficient, which depends on the density and atomic number of the material. The radiation dose of a single lumbar vertebrae or pelvis radiograph is around 0.7 mSv [34].

3.2 DUAL ENERGY X-RAY ABSORPTIOMETRY

DXA is a method which is used to measure a patient's areal (2D) BMD or bone mineral content (BMC) quantitatively. It is the golden standard to diagnose osteoporosis. In DXA imaging, two X-ray images are taken using two different X-ray energies. For example, with the GE Lunar Prodigy instrument (GE Lunar, Madison, WI), the mean energy levels are 38 and 70 keV [110]. Therefore, it is possible to solve mathematically the contribution of bone and soft tissue in the X-ray attenuation. Since the amounts of fat and lean tissue vary from patient to patient, the attenuation coefficient of soft

tissue is first calculated at a location adjacent to bone:

$$\begin{aligned} I'_1 &= I'_{0,1} e^{-M_\mathrm{l}\alpha_{\mathrm{l},1}} e^{-M_\mathrm{f}\alpha_{\mathrm{f},1}} \\ I'_2 &= I'_{0,2} e^{-M_\mathrm{l}\alpha_{\mathrm{l},2}} e^{-M_\mathrm{f}\alpha_{\mathrm{f},2}}, \end{aligned} \tag{3.2}$$

where I'_i and $I'_{0,i}$ are attenuated and unattenuated intensities at a location adjacent to bone for two different energy levels, M_j is the areal mass for lean (l) and fat (f), and α is the attenuation coefficient specific for each energy level and material. The ratio between the fat and lean tissue can be solved from a pair of equations (3.2) to obtain the attenuation coefficient for soft tissue α_s. Subsequently, areal BMD can be calculated from the measurements at bone site

$$\begin{aligned} I_1 &= I_{0,1} e^{-M_\mathrm{b}\alpha_{\mathrm{b},1}} e^{-M_\mathrm{s}\alpha_{\mathrm{s},1}} \\ I_2 &= I_{0,2} e^{-M_\mathrm{b}\alpha_{\mathrm{b},2}} e^{-M_\mathrm{s}\alpha_{\mathrm{s},2}}, \end{aligned} \tag{3.3}$$

where b denotes bone and s denotes soft tissue. Finally, BMD, *i.e.*, M_b, is

$$\mathrm{BMD} = \frac{\ln\left(\frac{I_2}{I_{0,2}}\right)\left(\frac{\alpha_{\mathrm{s},1}}{\alpha_{\mathrm{s},2}}\right) - \ln\left(\frac{I_1}{I_{0,1}}\right)}{\alpha_{\mathrm{b},1} - \alpha_{\mathrm{b},2}\left(\frac{\alpha_{\mathrm{s},1}}{\alpha_{\mathrm{s},2}}\right)}. \tag{3.4}$$

The errors due to geometric magnification during imaging are automatically corrected in current DXA devices (such as GE Lunar Prodigy and iDXA). Therefore a reconstructed DXA image is a parallel projection of the 3D object. The radiation dose of a total body scan is 0.004 mSv in older GE Lunar Prodigy instrument. In newer iDXA instrument this has increased to 0.03 mSv due to higher resolution (0.25×0.30mm versus $1.05x0.60$ mm). However, this is still less than one twelfth of that delivered in a hip radiograph [34].

3.3 COMPUTED TOMOGRAPHY

In CT imaging, a X-ray tube and detector are rotated around the patient and a sequence of X-ray images are taken from different directions around the patient [111]. In early days, pencil or fan-shaped X-ray beams were used, but modern CT devices commonly use spiral multi-detector or cone beam geometries [112]. A 3D attenuation map is reconstructed from the acquired images. Conventionally, the

reconstruction has been performed with back projection techniques. However, the use of iterative reconstruction methods is increasing since they enable the application of image correction techniques not possible with back projection. Reconstruction quality depends on the number of projections and the signal-to-noise ratio in each projection, which both are related to the radiation dose on the patient. Usually, the attenuation is presented as Hounsfield units (HUs), where -1000 is defined for air and 0 for water.

In QCT imaging, a CT calibration phantom is imaged at the same time with the patient. The phantom is used to compare the radiodensity of an unknown material to the radiodensity of dipotassium phosphate or hydroxyapatite, which are the most common calibration materials. The volumetric BMD of the object can be calculated from this relation. When volumetric BMD is known, it can be related to the mechanical properties of bone by using experimentally found relationships, *e.g.*, to its Young's modulus (E) [113–118]. Thereafter, this information can be used in FE modeling. One of the most widely used relations [115] is

$$E = 8920\rho_{\text{ash}}^{1.83} \tag{3.5}$$

where ρ_{ash} denotes the ash density of bone.

Several parameters derived from QCT, such as femoral neck cross-sectional area, femoral neck axis length and volumetric trabecular BMD at the neck or trochanter, have been shown to correlate with the strength of the proximal femur [119–121].

DICOM standard

Digital Imaging and Communications in Medicine (DICOM) is the standard for handling, storing, printing and transmitting information in medical imaging. DICOM images include both the medical image and information about the patient and the imaging parameters.

Figure 3.1 presents the coordinate system for 3D images in the DICOM standard [122]. This coordinate system is used in study V. The origin of the DICOM coordinates is placed arbitrarily and it is usually constrained on the device in use. The directions of the coordinate axes are constrained to the patient and therefore it is

called the patient-based coordinate system. X-axis points from the right hand to the left hand, Y-axis from anterior to posterior and Z-axis from the toes to head. Therefore, if the patient is turned from the supine to the lateral position during imaging, also the X and Y coordinates turn 90 degrees related to the imaging device. In the DICOM standard, field **ImagePositionPatient** defines the location of the center of the pixel in the upper-left corner of each 2D image slice. Field **PatientPosition** describes the positioning of the patient in the imaging device. The orientation of the image related to the patient coordinate system is defined in field **ImageOrientationPatient**. It is a 6x1 vector which the three first elements define the direction of the first row of the image and last three elements define the direction of the first column of the image according to the dicom coordinates.

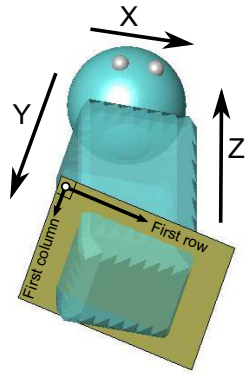

Figure 3.1: Coordinates used in DICOM standard. The origin is arbitrary. X, Y and Z axes are from the right hand to the left hand, from anterior to posterior and from inferior to superior. DICOM standard defines the center of top left pixel of a slice with these coordinates. Then it defines the orientation of the slice as the direction of first row and first column.

3.4 ULTRASOUND METHODS FOR OSTEOPOROSIS DIAGNOSIS

Ultrasound is also commonly used to determine bone quality. Radiographic methods mainly measure the BMD in two or three dimensions, whereas ultrasound information may be related more to the bone structure and the organic and inorganic composition [123].

Most commonly, the speed of sound and ultrasound attenuation are measured in heel, partly since it is an easy location to access and because its trabecular structure responds to bone loss in osteoporosis [124]. The agreement between calcaneal ultrasound measurement and fracture risk has been found to be similar than in femoral DXA based BMD, but the patient groups they classify as high risk partly differ [125]. In principle, ultrasound back-scatter methods allow measurements at osteoporotic fracture sites such as at the hip [126,127].

4 Mathematical Methods

Several mathematical methods were utilized in the present studies. They are shortly introduced in following sections.

4.1 LANDMARK POINTS

Landmark points are commonly used in morphometrics. They are points which preserve their correspondence between and within object populations [128]. Therefore, the location of a landmark can be recognized from all images taken from similar objects. In other disciplines, landmarks may be called by different names, *e.g.*, anchor points, control points or markers. Landmarks are commonly divided into three classes [128]:

1. Anatomical landmarks are locations which are biologically meaningful in an organism. An example is the tip of the minor trochanter in the proximal femur.

2. Mathematical landmarks are located in an image according to a mathematical or geometrical property of the object's shape or intensity. An example is the center of the femoral head, where the center is defined by fitting a ball inside the head.

3. Pseudo landmarks are points which are placed based on anatomical or mathematical landmarks. They can be placed for example with equal spacing on the surface of an object between two anatomical landmarks.

4.2 GENERALIZED PROCRUSTES ANALYSIS

Generalized Procrustes analysis (GPA) removes similarity transformations, *i.e.*, translations, rotations, reflections and scaling, between landmark sets [129]. Let X_i be the set of landmarks in p dimensions for the i:th patient or sample, and let $P_j^{(i)}$ be the j:th row of the X_i,

i.e., the j:th landmark. Then GPA minimizes the sum of square

$$e = \sum_{j=1}^{n} \sum_{u<v}^{m} \left\| P_j^{(u)} - P_j^{(v)} \right\|^2 . \tag{4.1}$$

where $\|\cdot\|$ is the Euclidean vector norm. In other words, GPA minimizes the sum of the distances from each landmark to the same landmark in the other objects.

The difference between ordinary and generalized Procrustes analysis is that in the GPA, the rotation is not aligned according to one of the samples but according to the average rotation when symmetry in the alignment is preserved.

In ordinary Procrustes analysis, the landmarks are aligned by first setting the mean of each column of X_i to zero in order to remove translation. Then the scale of each X_i is set to unity by normalizing the average distance from the origin to $P_j^{(i)}$ to one. Finally, the landmark sets are rotated to the position of one of the landmark sets by using a rotation matrix $R_i = UV^T$, where U and V are calculated with singular value decomposition (SVD)

$$X_1 X_i = USV^T, i \neq 1. \tag{4.2}$$

In GPA, an average rotation matrix is calculated between the landmark sets with several iterations.

4.3 THIN-PLATE SPLINE

Thin-Plate Spline (TPS) is an elegant tool for describing deformation in a whole image when the movements of n landmark points from location P_i to location V_i are known. In 1D, TPS is equivalent to cubic splines. It extends to 2D or 3D with only small modifications [130, 131].

TPS deformation is analogous to deformations in a thin metal plate. It minimizes the energy that is needed to bend the metal plate on the point constraints, *i.e.*, landmarks [130]. The bending energy of a metal sheet with small deformations follows a biharmonic equation $\Delta^2 U = 0$, where U is the solution of the equation:

$$U(r) = |r|^3 \qquad \text{in 1D,} \tag{4.3}$$

$$U(r) = r^2 \log(r^2) \qquad \text{in 2D, and} \tag{4.4}$$

$$U(r) = |r| \qquad \text{in 3D,} \tag{4.5}$$

where r is the Cartesian distance from the origin [130].

The TPS mapping $F(X)$ maps X from $\mathbb{R}^p$ to $\mathbb{R}^p$, where p is the dimension of the problem, *i.e.*, if X is $X = [x]$, $X = [x, y]$ or $X = [x, y, z]$, then accordingly $F(X) = f_x(X)$, $F(X) = [f_x(X), f_y(X)]$ or $F(X) = [f_x(X), f_y(X), f_z(X)]$. The calculation of TPS mapping $F(X)$ requires a few steps. First, the distance between two landmarks is defined as $r_{ij} = |P_i - P_j|$. The TPS transformation is constructed from two parts: a non-linear part where the bending energy is introduced and a linear transformations which introduces no work against elastic force. Matrix K forms the non-linear part and it includes the values of U for all paired combinations of the landmarks in their original position

$$K = \begin{bmatrix} 0 & U(r_{12}) & \cdots & U(r_{1n}) \\ U(r_{21}) & 0 & \cdots & U(r_{1n}) \\ \vdots & \vdots & \ddots & \vdots \\ U(r_{n1}) & U(r_{n2}) & \cdots & 0 \end{bmatrix}. \tag{4.6}$$

Matrix B forms the linear part which allows bending-free global rotations, translations, scaling and shearing of the object

$$B = \begin{bmatrix} 1 & P_1 \\ 1 & P_2 \\ \vdots & \vdots \\ 1 & P_n \end{bmatrix}. \tag{4.7}$$

The non-linear and linear parts can be combined as

$$L = \left[\begin{array}{c|c} K & B \\ \hline B^T & O \end{array}\right], \tag{4.8}$$

where O is a matrix including zeroes and ^{T} means matrix transpose. When the landmarks at transformed locations V (size $n \times p$, non-

linear deformations) are combined with $p \times p+1$ matrix of zeroes (introduces linear transformations) $Y = (V^T|O)^T$, the non-linear and linear coefficients of TPS mapping (W and A) can be calculated [130] by inverting L as

$$[W|A] = [L^{-1}Y]^T. \tag{4.9}$$

Hence, W and A include the coefficients of the bending and similarity transformations, and therefore their sizes are $p \times n$ and $p \times p+1$, respectively.

With help of the above equations the TPS mapping $F(X) = [f_1(X), \ldots, f_p(X)]$ in any point X along dimension j is defined as

$$f_j(X) = A_j[1|X]^T + \sum_{i=1}^{n} w_{ji} U\left(|P_i - X|\right), j = 1, \ldots p, \tag{4.10}$$

where A_j is the jth row of A and w_{ji} is the element at jth row and ith column of W . In other words, $F(X)$ defines where a point X moves to when the landmark points P are moved to the corresponding locations V, and the energy needed for bending is minimized. Proof for this theory can be found from [130].

Especially during optimization, it may be beneficial to change the direction of TPS mapping and role of landmark points P and V. In this formulation, the TPS map describes from which location the intensities or other information on the original image must be taken when the location is known in the result image. The benefits in this formulation are as follows. The locations of the points X in the result image can be determined to form a grid since they do not move. Secondly, if TPS is used several times, the inverse of L needs to be calculated only once since now source landmark points do not move. Lastly, it can be showed [131] that V_i in TPS is differentiable, which enables to use gradient-based optimization algorithms with TPS.

In Figure 4.1, a set of landmarks is located at the 2D contour of the femur. In the second image, the femoral neck-shaft angle is decreased by 10°, and the landmarks at the femoral head are moved accordingly. In addition, the landmark at the lateral side of the distal shaft is moved one centimeter in the lateral direction. The rest of the second image is deformed according to the deformation

field $f(X)$ from TPS.

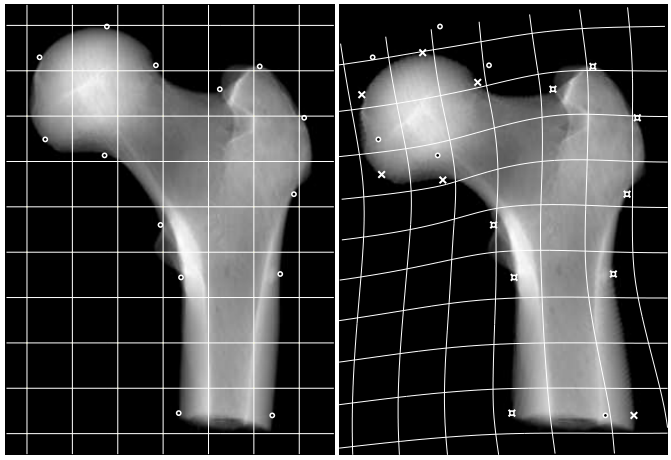

Figure 4.1: Image of a proximal femur before and after it is deformed with TPS. Deformation is defined by rotating the neck axis by 10 ° and by moving the landmark at the lateral side of the distal shaft one centimeter in the lateral direction. The grid in the second image has also been deformed according to the deformation field calculated with TPS

4.4 PRINCIPAL COMPONENT ANALYSIS

Principal component analysis (PCA) aims to simplify multivariate data. It is a statistical technique which describes a set of correlated variables with a smaller number of linearly independent variables called principal components, eigenvalues or modes. PCA was first invented by Karl Pearson in 1901 [132] and later invented independently by Hotelling [133]. Many research fields have their own name for PCA. Mathematically, PCA is an orthogonal linear transformation that maps the data into a new coordinate system. In this new coordinate system, the first coordinate axis is aligned with the direction of the largest variance of the data. The second axis is orthogonal to the first one, and aligned with the second largest direction of variation, and so on.

In PCA, observation data is collected into one matrix X, where each row includes the data of one variable, *e.g.*, from one sensor, and each column includes data from one object. X is centralized by diminishing the mean value of the observations from each row of

X. The principal components of the matrix X are usually calculated with SVD

$$X = USV^T \tag{4.11}$$

where U and V are the right- and left-hand eigenvectors and therefore orthonormal matrices, and the diagonal matrix S includes the eigenvalues. The many effective algorithms for solving SVD explain its popularity. The principal components of X can be calculated with

$$Y = U^T X \tag{4.12}$$

and if a set of principal components Y is given, then the original observation can be reconstructed by $X = UY$.

The strength of PCA is that when the SVD is truncated (which means that only L from the most significant principal components (Y_L) are used) the resulting observation matrix $X_L = UY_L$ is the nearest possible matrix to X with rank L. The matrix X_L is the nearest to X in the sense that the Frobenius norm between the X and X_L is the smallest possible one [134].

4.5 STATISTICAL SHAPE AND APPEARANCE MODELS

The shape and density of human organs vary between individuals. Statistical shape modeling (SSM) is a method that interprets this variation seen in medical images [135–137]. SSM contains a statistical model of the shape, which represents any shape of the object with a vector of a few varying scalar values. If also density information is included into the model, it is called the statistical appearance model (SAM) [138]. Both SSM and SAM are mathematically based on PCA.

In SSM, the shape of the object is represented with a set of points called nodes. In 2D, they are distributed over the contour of the object and in 3D over the surface of the object. The nodes are connected in 2D with lines called edges which produce the contour. In 3D, the triangles called faces produce the surface. This description of the average object is then deformed to the shape of each individual object in the training set of SSM, for example, with the help of landmarks and TPS. SSM requires that the node sets are isotopological, *i.e.*, the anatomical location of each node is preserved in all

individual shapes.

Each isotopological coordinate of each node of SSM represents one measurement or variable in PCA. Therefore, for a 3D object with m nodes and n samples or images, the size of the observation matrix $X = [x_1, x_2, \cdots, x_n]$ is $3m \times n$, where x_i is the ith individual. The translation, scaling and rotation between the nodes can be removed with GPA. Finally, the mean value of each coordinate between the individuals $\overline{x}$ must be removed from X. After PCA is applied to X, it can be represented as

$$X = \overline{x} + UY, \tag{4.13}$$

and each individual can be approximated using the equation

$$x_i = \overline{x} + Uy_i, \tag{4.14}$$

where U and Y originate from PCA. Variable Y has size $L \times n$, where L is the number of shape parameters, and it includes the values of shape parameters for each individual in the training set of SSM. The values of Y are easier to interpret if they are scaled with SD of the samples, *i.e.*, shape parameter b for an individual is

$$b = y/\ \mathrm{SD}(Y). \tag{4.15}$$

The appearance can be included into the model by adding nodes also inside each object and by representing the interior with triangles in 2D and with tetrahedrons in 3D, which are called elements. A density value for each element g_{im} can be captured when the digital image is treated as a step function and it is integrated over each element [116]. The q density values can be set after the node coordinates in X, when the size of X is $3m + q \times n$. Since nodes and densities have different scales, X needs additional normalization X, *i.e.*, $X = X/\,\mathrm{SD}(X)$. Otherwise the usage of PCA is similar as described earlier and follows the equation 4.14. A few instances of SAM of the proximal femur are presented in Figure 4.2.

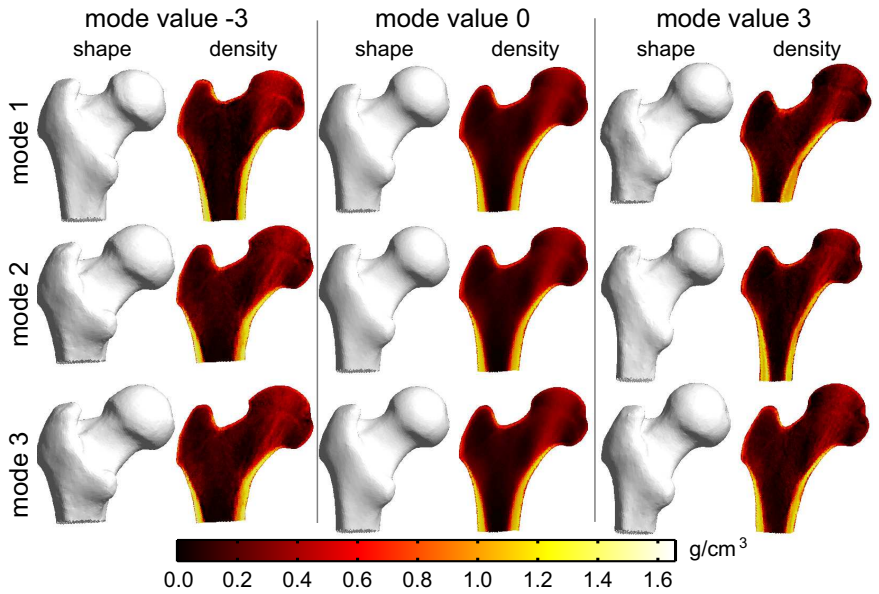

Figure 4.2: Three first modes of variation for the shape and density of a femoral SAM, when the mode values are varied between -3 and +3 standard deviations.

4.6 ARTIFICIAL NEURAL NETWORKS

Artificial neural networks (ANN) represents a machine learning technique, which is designed to mimic the function of the central nervous system of a human being. ANN can be used for example for function fitting, pattern recognition, data clustering or time series analysis. The first ANN that combined the function of human brains and mathematical logic was introduced in 1943 [139]. However, nowadays the development of ANN has moved far from its living counterpart and its recent development has been mostly based on the theories of signal processing and statistics [140].

The strength of ANN is that it is able to approximate any multidimensional nonlinear function [141]. ANN is also noise tolerant and is able to learn without supervision [140]. This means that no prior information or model about the modeled system is needed. Simply a large input and output data will suffice. The ANN's cores are (artificial) neurons that are interconnected together (Figure 4.3). Each neuron takes in one or multiple signals, which come from inputs or from other neurons, weights them with positive or negative

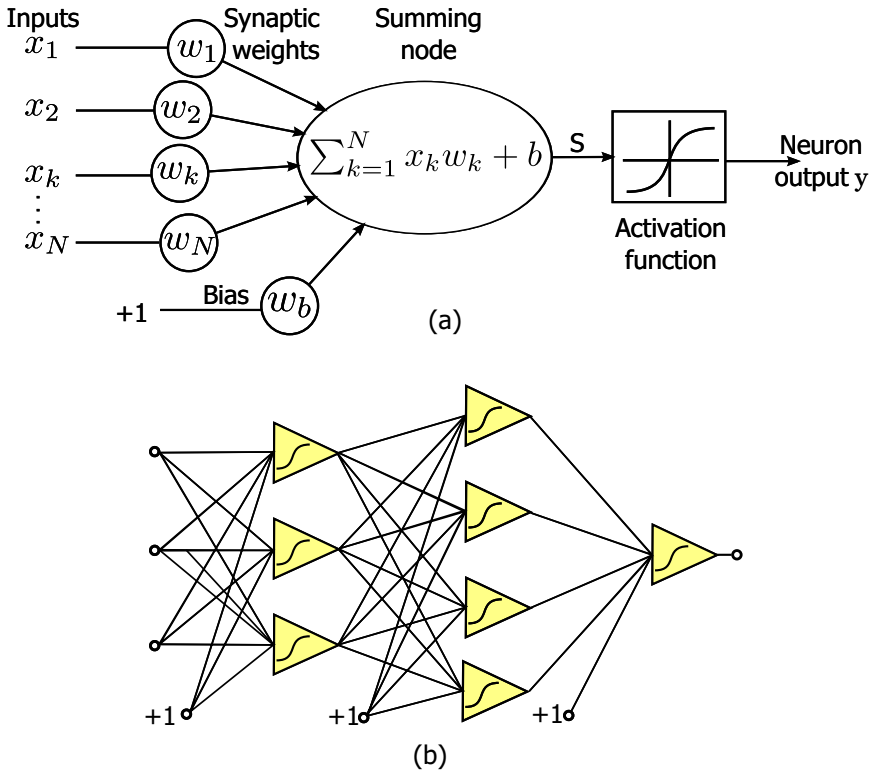

Figure 4.3: (a) A neuron of ANN has three main parts: synapses (inputs), accumulator and activation function. In the accumulator, the inputs are weighted with positive or negative weights and thereafter summed together with a bias term. The sum is then fed to an activation function which produces the output signal of the neuron. (b) An ANN with simple multilayer perceptor architecture. This ANN has three inputs, three neurons in the first hidden layer, four neurons in the second hidden layer and one neuron in the output layer.

weight and then sums them up. The resulting summed signal is then augmented or reduced by an activation function, which shape can be for example linear bipolar, thresholding or sigmoidal, depending on the architecture of the ANN [140].

Connections between the inputs, neurons and output(s) form the network. The most widely used and the oldest architecture of ANN is multilayer perceptor (MLP) [142]. In this topology, the neurons are aligned into layers and each neuron in a layer is connected only with the neurons in the layers next to it (Figure 4.3). The benefit of this kind of architecture is that it is implemented in all neural networks software, including Matlab, although other architectures also exist. For example, in the bridged multilayer perceptor, the neurons are connected over layers and in a fully connected cascade architecture, the neurons are set into series such that all neurons are connected with each other and with the input and output [142]. The benefit of these architectures compared with MLP architecture is that less neurons and connections between neurons are needed to model a complex system. As a downside, all ANN software are not able to train these other types of architectures [142, 143].

Normal feed-forward ANN (which means that ANN does not include feed-back loops) is most commonly trained with the error back propagation method [141]. In this method, ANN is set parallel with the modeled system and the error e, for example, the mean square error, between the output of ANN and the original system is calculated. The error e can be presented as a function of all weights w of all the neurons $e(w_i)$, $i = 1 \dots M$ where M is the number of neurons times the number of weights in one neuron. The error e can then be minimized, for example with the method of steepest descent or the Levenberg-Marquardt algorithm [141].

4.7 GENETIC ALGORITHM

Genetic algorithm (GA) is a computational method that solves both constrained and unconstrained optimization problems. It is based on natural selection and evolution, first introduced by Charles Darwin [144]. During optimization, GA utilizes processes found in nature such as inheriting, mutation, selection and recombination [145].

GA usually starts with a random population of individuals. In practice, an individual i is a vector of scalar values x_i, which is often called the chromosome. The function F, which one optimizes, is a function of x, and therefore $F(x_i)$ gives a score for an individual i. The scores are then used to rank the individuals. Based on a selection rule, some of the best individuals are defined as the elite and fed as children to the next iteration round. The worst individuals are abandoned and the rest of the children are created by recombining the parents. Some of the parents are mutated during recombination based on a stochastic rule in order to create new combinations. In addition, new random children can be created. The iteration is continued until one of the stopping criteria, such as maximum number of iterations or a score below a set threshold, is achieved [145, 146].

4.8 DIGITAL IMAGE CORRELATION

In a digital image correlation (DIC) technique, the surface strains of an object under loading are measured optically [41, 147]. The surface is covered with a random dot or some other optically visualizable pattern, and the object is imaged with one or several digital cameras (Figure 4.4). First, the initially captured image is divided into small elements each of which has unique patterns. Then surface images are captured at constant time intervals during loading. At each time interval, the captured image is correlated with the initial or previous image in order to obtain element displacements. If two or more cameras are used, the recorded displacements are not restricted to 2D, but the 3D surface and thus 3D displacements of the object can be reconstructed. The 3D element locations are computed from the stereo view of the cameras using rules obtained from stereography ([41]).

The strains can be calculated from surface displacements. For each traced point, the two closest neighbors are found and triangles are formed by combining these points. Rigid transformations are removed by first transforming both initial and deformed triangles into an xy plane such that the base vertex moves to the origin and the vector from the base vertex to the first neighbor is aligned with the x-axis. Thereafter, motion between the vertices ($\mathbf{P}$ and $\mathbf{Q}$) at the

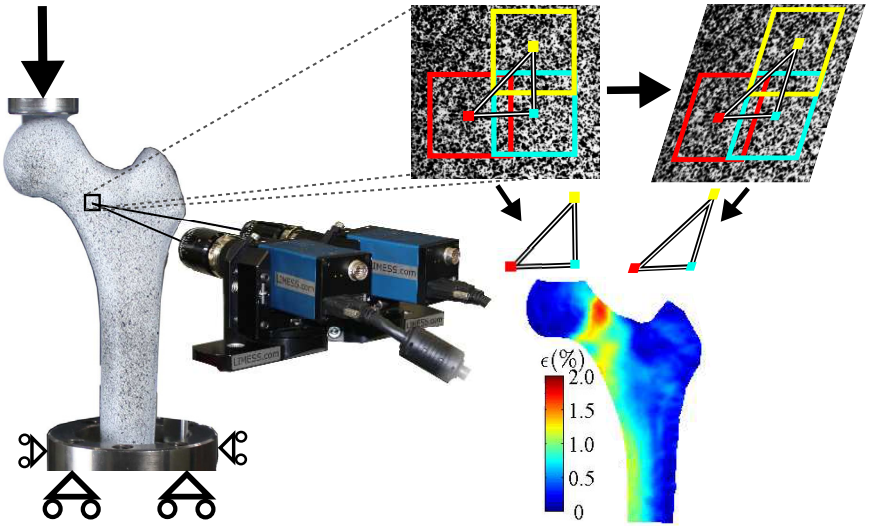

Figure 4.4: DIC principle. Two cameras track the object surface during loading. The surface has been painted with a pattern which makes it possible to track surface movements during stress. When the tracked points are divided into triangles, the strains on the surface can be calculated.

initial triangle and vertices (**p** and **q**) at the deformed triangle can be described with linear mapping ϕ as

$$\begin{aligned} \phi_1 &= a_{11}X_1 + a_{12}X_2 \\ \phi_2 &= a_{21}X_1 + a_{22}X_2 \end{aligned}, \tag{4.16}$$

where

$$\mathbf{A} = \begin{pmatrix} a_{11} & a_{12} \\ a_{21} & a_{22} \end{pmatrix} = \begin{pmatrix} p_1 & q_1 \\ p_2 & q_2 \end{pmatrix} \begin{pmatrix} P_1 & Q_1 \\ P_2 & Q_2 \end{pmatrix}^{-1}. \tag{4.17}$$

Then deformation gradient tensor **F** can be calculated as

$$\mathbf{F} = \frac{\partial \phi}{\partial \mathbf{X}} = \nabla \phi. \tag{4.18}$$

The right Cauchy-Green deformation tensor **C** is

$$\mathbf{C} = \mathbf{F}^T\mathbf{F}. \tag{4.19}$$

Finally, the Lagrangian strain tensor **E** can be calculated as

$$\mathbf{E} = \frac{1}{2}\left(\mathbf{C} - \mathbf{I}\right). \tag{4.20}$$

In **E**, the strains in the directions of the x- and y-axes are $E_{11} = \epsilon_{xx}$ and $E_{22} = \epsilon_{yy}$, respectively, and the shear strain is $E_{12} = E_{21} = \epsilon_{xy}$ [147]. All other strains can be calculated from these strains. For example, the first and second principal strains are the eigenvalues of **E**, and they describe the amount of strain in the directions of the highest (tensile) and lowest (compressive) strain. Von Mises strain ϵ_v, which gives a measure of total strain, can be calculated as

$$\begin{aligned}\epsilon_v = \Bigg(\frac{1}{2}\Big[&(\epsilon_{xx} - \epsilon_{yy})^2 + (\epsilon_{yy} - \epsilon_{zz})^2 \\ &+ (\epsilon_{zz} - \epsilon_{xx})^2 + 6(\epsilon_{xy}^2 + \epsilon_{yz}^2 + \epsilon_{zx}^2)\Big]\Bigg)^{\frac{1}{2}},\end{aligned} \tag{4.21}$$

which in a 2D case can be simplified to

$$\epsilon_v = \sqrt{\epsilon_{xx}^2 - \epsilon_{xx}\epsilon_{yy} + \epsilon_{yy}^2 + 3\epsilon_{xy}^2}. \tag{4.22}$$

If the vertices are close to each other, they are noise-sensitive; this noise can be reduced by using spatial averaging for the calculated strains.

Even though DIC is a well recognised method in other disciplines [148, 149], it is not widely used in biomechanics. It is more common to measure surface strains only locally with strain gauges [26, 66, 150, 151]. Recently, the strains of the proximal femur have been measured in 2D [152], but unfortunately 2D strains only provide a qualitative validation of 3D FE models. In 3D, strains have been measured in rat femurs [153] and in one composite femur [154]. Recently, human cadaver femurs were measured with DIC in the side-fall configuration [155].

4.9 FINITE ELEMENT MODELING

In addition to experimental tests, the mechanical behavior can be studied by using numerical modeling. The first finite element (FE)

model of bone was developed at the beginning of the 1970s [156]. In FE modeling, the geometry is divided into small regions called elements, which are assembled together. Usually, these elements are tetrahedra or hexahedra, and inside an element, the material properties are constant. Each element can experience three different compressive or tensile stresses or strains and six shear stresses or strains. Hooke's law mathematically describes the relation between the stresses and strains for a linear elastic material as

$$\sigma_{i,j} = \sum_{k=1}^{3} \sum_{l=1}^{3} c_{ijkl} \epsilon_{kl}, \tag{4.23}$$

where i and j are 1, 2 or 3, and c_{ijkl} is the elastic coefficient. Since the elements are small, the shear stresses are symmetric (for stresses $\sigma_{ij} = \sigma_{ji}$, when $i \neq j$); this symmetry yields in total six different strains and stresses. In the tensor form, equation (4.23) would be

$$\vec{\sigma} = \mathbf{C}\vec{\epsilon} \tag{4.24}$$

where $\vec{\sigma} = (\sigma_{11}, \sigma_{22}, \sigma_{33}, \sigma_{12}, \sigma_{13}, \sigma_{23})^T$, $\vec{\epsilon} = (\epsilon_{11}, \epsilon_{22}, \epsilon_{33}, \epsilon_{12}, \epsilon_{13}, \epsilon_{23})^T$ and $\mathbf{C}$ is the stiffness matrix.

In the case of linear isotropy, the material has the same properties in any direction, when the stiffness matrix has a reduced form

$$\mathbf{C} = \frac{E}{(1+\nu)(1-2\nu)} \begin{pmatrix} 1-\nu & \nu & \nu & 0 & 0 & 0 \\ \nu & 1-\nu & \nu & 0 & 0 & 0 \\ \nu & \nu & 1-\nu & 0 & 0 & 0 \\ 0 & 0 & 0 & 1-2\nu & 0 & 0 \\ 0 & 0 & 0 & 0 & 1-2\nu & 0 \\ 0 & 0 & 0 & 0 & 0 & 1-2\nu \end{pmatrix}, \tag{4.25}$$

where E is Young's modulus and ν is Poisson's ratio. Since the shear (G) and bulk (K) moduli can be expressed with Young's modulus and the Poisson's ratio $\left(G = \frac{E}{2(1+\nu)}, K = \frac{E}{3(1-2\nu)}\right)$, two independent variables describe a linear isotropic material.

A common flow diagram describing the procedure required for the construction of an FE model of a whole bone is presented in Figure 4.5.

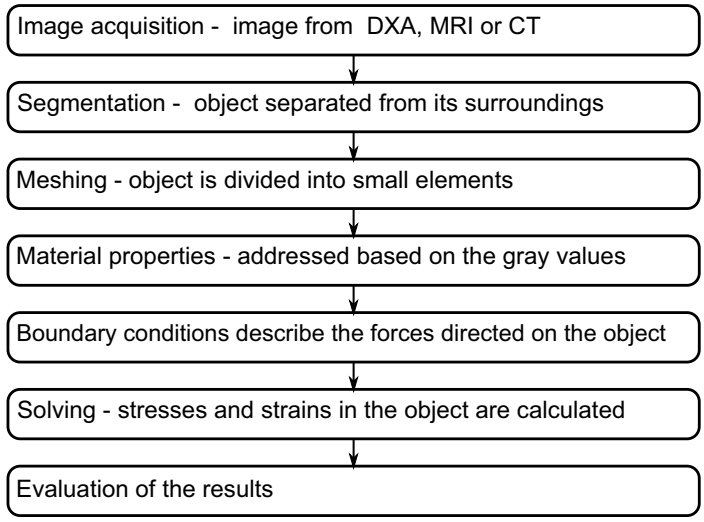

Figure 4.5: Common flow diagram of FEM construction.

Imaging and segmentation

The first step in the building of an FE model is to acquire the geometry of the object. Provided that the model is built based on a CT or MR image, the object must be extracted from the image by segmentation. The outer surface is necessary although internal structures such as the boundary between the cortical and trabecular bone are important. If the image quality is good and the border between the object and the surrounding tissue is well-defined, the segmentation can be done automatically by utilizing thresholding, basic image processing tools, Boolean operations and regional properties, among others. Otherwise, manual segmentation may be needed.

Meshing

In meshing, the segmented geometry is divided into a collection of simple subdomains called elements, with vertice points that are called nodes. The adjacent faces of the neighboring elements must share their vertices. The size of the elements can be constant over the whole geometry. However, to reduce the computational effort,

the element size can be varied from site to site depending on how exact the calculations are needed in that specific region. For example, in the femur, the element size is often smaller in the epiphyses than in the diaphysis [25]. Several commercial or open source tools such as Mimics (Materialise, Leuven, Belgium), Hypermesh (Altair Engineering, Inc., USA), Ansys ICEM (Ansys Inc., Cannonsburg, PA, USA) or CGAL mesher, can be used for mesh generation.

There are many metrics which can be used to measure tetrahedral mesh quality. These measures are often normalized using a scale ranging between 0 and 1. Then, the measure approaches zero for a poorly-shaped tetrahedron and attains the maximum value of unity for the regular tetrahedron. The solid angle of a vertex of a tetrahedron defines the area which is bordered on the surface of a unit sphere when the sphere is centered at the vertex and the other vertices are projected on its surface. The minimum solid angle θ_{min} is the smallest of these [157]. The solid angle can have values between 0 and 2π and therefore it can be scaled on $[0, 1]$.

Other common metric is the radius ratio ρ, which is the ratio between inradius and circumradius of a tetrahedron [157]. The aspect ratio of a triangle is defined as the length of the longest edge divided by the orthogonal distance from the edge to the third vertex. The aspect ratio can have values between 1 and infinity [158, 159]. As a rule of thumb, aspect ratios over 40 are usually closely examined but numeric round-off errors should start to appear only when the aspect ratio exceeds 1000 [159].

Material properties

In order to extract material properties for a bone FE model, the vBMD values of a 3D QCT image can be converted to Young's moduli values based on experimentally determined relationships [160], such as that described in equation (3.5). Several strategies are used for extracting a Young's modulus value from an image for each element. The simplest approach is to find the closest voxel for each element or to calculate a weighted average of the closest neighbors [118]. A more sophisticated, and often more accurate, approach is to treat the image as a piece-wise linear 3D equation and to calculate numerical integral over this equation or its approximation at the region of each element [116, 117].

Boundary conditions

The mechanical environment is applied to an FE model by altering its boundary conditions. Boundary conditions describe restrictions of the movement and the displacements or forces that are directed on the object. For example, if the aim of the simulation is to reproduce a mechanical testing experiment, the forces and displacements recorded during the experiment are applied to the model.

Solving

When the boundary conditions are known, an FE solver calculates the partial differential equation, which describes the mechanics of the model. It finds the best solution for all elements where the nodal values match between adjacent elements. For example, Ansys and Abaqus are commonly used in biomechanics to solve the simulated mechanical conditions imposed on the model.

Evaluation of the FE result

Evaluation of the results depend on the purpose of the modeling. For example, it can be a validation of the model against an experiment, finding a deeper understanding about the internal forces in bone, or predicting the behavior of bone under extreme conditions [161]. Part of the evaluation is the visualization of the stresses and strains on the surface or in the intersection of the femur. For validation, the stiffness of the whole geometry or surface strains of the model can be compared with those from an experiment with similar boundary conditions and proper surface strain measurements, such as strain gauges or DIC [64,162].

Modal assurance criterion (MAC) compares displacements between two models or between a model and an experiment with a large amount of data [163,164]. The comparison is performed globally, and MAC returns one scalar value which is comparable with correlation coefficients. The MAC value is more sensitive to large differences and relatively insensitive to small ones [165]. The MAC

is calculated as

$$\mathrm{MAC}(\phi_i^{(1)}, \phi_j^{(2)}) = \frac{\left((\phi_i^{(1)})^T m^{(k)} \phi_j^{(2)}\right)^2}{\left((\phi_i^{(1)})^T m^{(k)} \phi_i^{(2)}\right)\left((\phi_j^{(1)})^T m^{(k)} \phi_j^{(2)}\right)} \tag{4.26}$$

where $\phi_i^{(1)}$ is the displacement vector of the i^{th} timestep of model 1, $\phi_j^{(2)}$ is the displacement vector of the j^{th} timestep of model 2, and $m^{(k)}$ is the diagonal of the mass matrix. When the nodes between the models are matched by finding the nearest neighbor between each node, k is 1 in (4.26), and when the nodes are matched by interpolating their values from model 1 to model 2, the value of k is 2 [159]. If the mass matrix is not available, such as in the stationary case, all displacements have equal weight [159].

4.10 3D SHAPE RECONSTRUCTION BASED ON 2D IMAGES

If the 3D shape of the object is reconstructed based on the 2D image, the same analyses and interpretation techniques which are usually valid only with CT or MR images can also be used with 2D images [166]. Therefore, methods which register the pre-captured 3D image or a shape model and 2D image(s) have been explored [166]. However, most commonly, the aim of these methods is to perform an intra-subject registration where pre-interventional CT or MRI image is aligned with intra-interventional 2D image(s), most commonly using rigid registration [166–169]. These kinds of methods are critical, for example, for image-guided endoscopy [170] and image-guided surgery [171]. However, they are not suitable for reconstructing a new unknown 3D shape, even though similar sub-parts are used in both approaches, such as the correspondence calculation between the 3D and 2D images during the registration [166].

Reconstruction of the 3D femoral shape and density based on solely 2D information is not possible. Instead, some prior information is needed. A straightforward way to implement this information is to use rules regarding shape. For example, these can be that the shaft is defined to be circular [172] or the femoral head can be defined to be a half sphere [40]. A more common ap-

proach is to use a general shape template, which includes information about the average shape of the object, or to utilize a statistical model which includes information about both the average shape and the shape variations between individual objects. The shape for a general shape template can be obtained with visual evaluation where the bone in a training set with the most average features is chosen [35, 173–175]. Another option is to choose a bone with the most average shape parameters [40, 176] or based on similarity measures between the training bones and the bone in the 2D image [38]. One can also use the mean shape of the training bones as the template [36]. The SSMs [177–180] and SAMs [181, 182] are the most common statistical models used as templates. The information about the density distribution can be implemented in SAMs voxel by voxel [182–184], or by giving a density value for each element or node in SAM [185]. The density variation inside each element can also be described with a function, for example, with the Bernstein polynomial [181, 186, 187].

The general shape or SSM template and 2D image(s) can be registered by using features usually identified as landmarks [36] or extracted bone contours [35, 173, 175, 176, 179]. On the contrary, SAM-based templates are usually registered using intensity based registration [39, 181, 188]. In intensity-based registration, the similarity between digitally reconstructed radiographs [189] (described in more detail in section 6.4.1) created from the 3D template and the 2D images is maximized. Intensity-based registration has also been used with SSM-based templates, but in that situation the density information in the SSM has to be implemented based on an average distribution [190] or it is based on the cortical thickness [191].

Usually, at least two projections from the object are used in the 2D-to-3D reconstruction [35, 173, 175–177, 179, 186]. Two or more projections enable some information in all three dimensions about the shape and the density of the object. On the contrary, when reconstruction is based only on one projection [36,38,40,182], no information is available about the direction perpendicular to the projection plane. Therefore, the reconstruction relies fully on *a priori* information about this direction. On the other hand, the benefits are that the dose during imaging can be minimized and also devices where multi-view imaging is not possible can be used for the

reconstruction. In general, including a second projection in the reconstruction significantly increases its accuracy, whereas adding a third or additional projections provides only a marginal additional improvement in the accuracy [183,190]. Most commonly, the reconstruction is done using X-ray images [36,38,40,173,175–177,179,180], but also DXA-based methods have been introduced [35, 182]. Projected CT images have been used as reference images [186] mostly to evaluate some methodological aspects.

5 Aims of the present study

The main aim of this thesis was to develop a method that would be able to reconstruct the 3D shape and internal density of the proximal femur from a single 2D DXA image.

The specific aims of this thesis were:

- To evaluate the accuracy of the reconstruction and its effect on the outcome of FE modeling
- To develop a method that would be able to estimate 3D rotation of the femur in a 2D radiograph
- To evaluate the strength of the proximal femur by measuring full surface strains with the digital image correlation method
- To automatize the method to reconstruct the 3D shape of the proximal femur and to further automatize the development of patient-specific FE simulations based on the reconstructed shape.

6 Materials and Methods

This thesis consists of five independent studies (I-V). Materials and methods used in the studies are summarized in table 6.1.

Table 6.1: Materials, imaging and methods used in studies I-V. The samples/subjects used for the different image-sets are divided into sets A-F.

Study	Samples	Imaging	Method
I,II	Proximal cadaver femurs (A)	CT, (DXA)	Training and testing of 2D-to-3D reconstruction and FE analysis
III	Proximal cadaver femurs (A)	CT	Training set for estimation of femoral 3D orientation
	Cadaver femurs (B)	CT	Training set for estimation of femoral 3D orientation
	Femurs from clinical subjects (C)	CT	Testing set for estimation of femoral 3D orientation
IV	Composite femurs (D)	CT, DIC	Mechanical testing experiment
V	Proximal cadaver femurs (A)	CT, DXA	Training and testing of 2D-to-3D reconstruction and FE analysis
	Pelvises from clinical subjects (E)	CT	Training of 2D-to-3D reconstruction
	Pelvises and femurs from clinical subjects (F)	CT, DXA	Testing of 2D-to-3D reconstruction and FE analysis

6.1 SUBJECTS, SAMPLES AND IMAGING

The material sets have been summarized in table 6.2. All sets were imaged with a CT device. The CT devices and the parameter settings used during imaging are listed in table 6.3.

Cadaver proximal femurs (A)

Sample set A consisted of proximal cadaver femurs (Table 6.2), which have been collected at Kuopio University Hospital starting from 2008. Ethical approval for the collection of samples was granted by the National Authority for Medicolegal Affairs (permission number: 5783/04/044/07). None of the cadavers had any pre-existing conditions that might have affected bone metabolism. The collection of the femurs continued during the studies and therefore the number of samples increased from study I-II to study III and V. The femurs were scanned using a CT device (Table 6.3). A CT calibration phantom (Mindways Software Inc.,Austin, TX, USA) with known dipotassium phosphate (K_2HPO_4) content was scanned simultaneously with the bones. It was first used to calibrate the CT numbers to BMD and thereafter the BMD values were mapped to Young's moduli using equation (3.5). The femurs were also imaged with GE Lunar Prodigy DXA scanner (GE Healthcare, Madison, WI) using resolution 1.05×0.60mm. In addition, eleven of the newest bones were imaged with GE Lunar iDXA DXA scanner with resolution 0.25×0.30mm.

Table 6.2: Samples used in studies I-V. The sample sets were: (A) cadaver proximal femurs, (B) cadaver femurs, (C) femurs from clinical subjects, (D) composite femurs, (E) pelvises from clinical subjects and (F) pelvises and femurs from clinical subjects.

Study	**Samples**	**n**	**Ages mean±SD (min-max)**	**Gender M**	**F**	**BMD (g/cm^2)**
I,II	A	18	52 ± 15 (26-82)	16	2	0.869 ± 0.165
III	A	24	52 ± 15 (18-82)	20	4	0.897 ± 0.171
	B	9	-	-		-
	C	19	-	6	4	-
IV	D	6	-	-		-
V	A	37	49 ± 16 (18-82)	33	4	0.892 ± 0.160
	E	47	89 ± 8 (39-74)	29	19	-
	F	14	75 ± 3 (69-78)	0	14	0.785 ± 0.105

Table 6.3: CT devices and their imaging parameters used in studies I-V. The sample sets were: (A) cadaver proximal femurs, (B) cadaver femurs, (C) femurs from clinical subjects, (D) composite femurs, (E) pelvises from clinical subjects and (F) pelvises and femurs from clinical subjects. Radiation dose is measured with volumetric CT dose index ($CTDI_{vol}$)

Sample set	Device	Tube Voltage (kV)	Exposure (mAs)	$CTDI_{vol}$ (mGy)	Resolution (mm)
A	Siemens Definition AS	120	210	16	0.4-0.6
B	Siemens Definition Flash	120	300	29	0.4-0.2
C	Siemens Definition AS+	120	52	4	0.7-0.8
D	Siemens Definition Flash	120	300	29	0.2-0.3
E	Philips Ingenuity CT	140	63	6	0.5-0.9
F	Philips Precedence 6P	120	100	-	0.7-2.0

Second cadaver femur set (B)

The second cadaver femur set (B) was collected at the Erasmus University Medical Center in Rotterdam (Table 6.2). The set of nine femurs originated from seven donors. The bones were imaged with a CT scanner (Table 6.3). No medical history was available.

Femurs of clinical subjects (C)

The third set (C) included hip CT images from clinical subjects (Table 6.3). The subjects were originally imaged for vascular examination. Both left and right femurs in the ten CT images were used, except one femur that was partly outside the field of view and was therefore excluded from the set.

Composite femurs (D)

Six fourth generation medium-sized left composite femurs (D) (model number: 3403) from Sawbones (Pacific Research Laborato-

ries, Inc., Vashon Island, WA, USA) were acquired for a mechanical testing experiment. The bones were imaged with a CT scanner (Table 6.3).

Pelvises of clinical subjects (E)

Pelvises of 32 total hip arthroplasty patients (E) were imaged with a CT scanner (Table 6.3) prior to operation. The CT images of the pelvises contralateral to the arthroplasty were used in study V.

Pelvises and femurs of clinical subjects (F)

The last set (F) included left pelvises and femurs of 14 women from Osteoporosis Risk Factor and Prevention Study (OSTPRE) cohort [192, 193]. The left hips of the subjects were imaged with a CT device (Table 6.3) and with GE Lunar Prodigy DXA scanner [127]. The study was approved by Kuopio University Ethical Committee (Decision 80/2008).

Preprocessing of the CT images

In studies I-III, the cadaver femurs were segmented with a custom-made software written in Matlab, where the size of the voxels were equalized in the images by resizing them to isotropic voxels of size 0.6 mm and the femurs were segmented using threshold of 1285 HU (0.89 g/cm^3). Thereafter, uniform femur images were created by filling the gaps on the femur surface with an image closing operation. Thereafter the gaps in the interior were filled with a hole detection algorithm in Matlab.

The proximal cadaver femurs were preprocessed again for study V. The images were resized to isotropic voxel size of 0.4 mm and segmented using Mimics (version 15.1, Materialize, Belgium). The CT images of the clinical subjects in studies III and V were also segmented using Mimics.

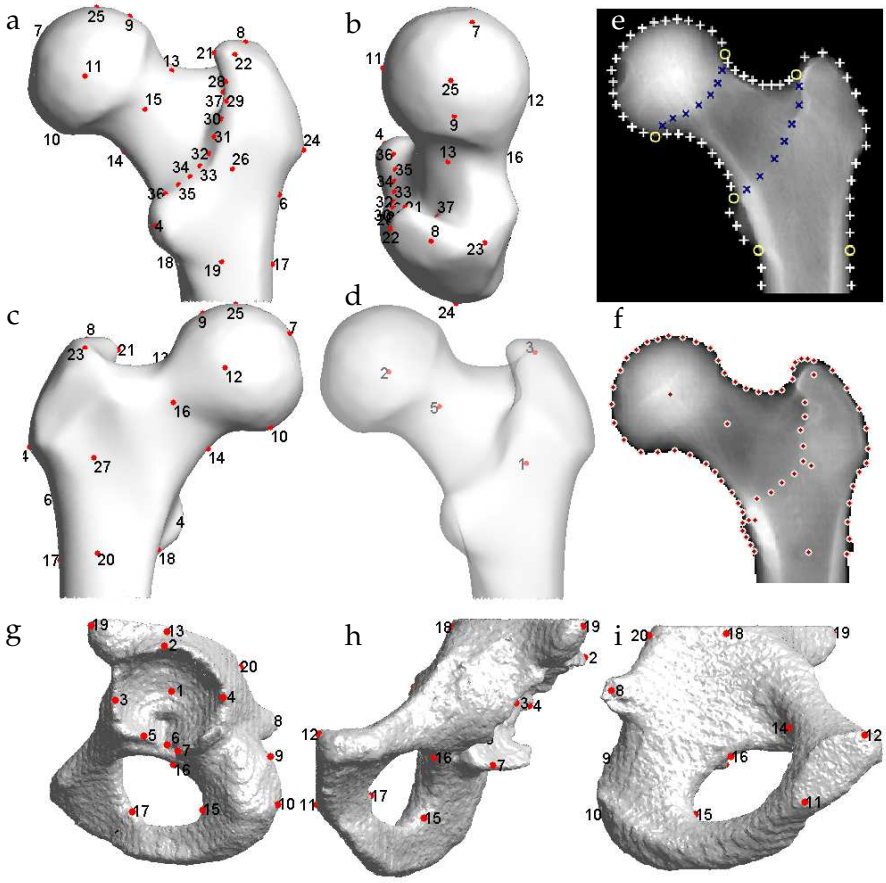

Figure 6.1: Landmarks on the 3D femur from different views (a-d). The 2D landmarks in studies I and III (e-f). Landmarks on the pelvis from different views (g-i).

6.2 LANDMARKS

6.2.1 3D landmarks

After segmentation, a set of landmarks was placed on the proximal femurs using semiautomatic software in Matlab. First the center of the distal shaft, the tips of the minor trochanter, the head and the proximal trochanter were located manually from the 3D rendering of the femoral surface. Thereafter the femoral shaft was aligned vertically. Subsequently, the code placed all other landmarks automatically. The landmark locations are presented in Figure 6.1 and the locations are listed in detail in the original studies II, III and V.

In studies I-II and IV, the first 27 landmarks were used for the femur. In study III, landmarks 28–36 were added onto the boundary between the neck and trochanter to capture the effect of rotation on the width of the projected major trochanter. In study V, landmark 37 was included into the set of the first 27 landmarks in order to guarantee smooth mesh warping during building of the femoral statistical appearance model (SAM) in the region of the superior trochanter.

The landmarks 1-12 and 14-17 on the pelvis were set manually using a custom-made graphical user interface in Matlab. Landmarks 13 and 18-20 were set automatically based on the manual landmarks and surface features. The landmarks are presented in Figure 6.1.

6.2.2 2D landmarks

Two-dimensional landmarks were set on the projected CT images of the femur and on the DXA images of the cadaver femurs. In study I six anatomical landmarks were set on the contour (Figure 6.1) and then mathematical landmarks were placed between them. In study II, the femoral 2D landmarks 1–27 were set on the projected CT images and DXA images semi-automatically. The locations of the 2D landmarks corresponded to the projected locations of the 3D landmarks. In study III, the 2D landmarks were set on the projected femoral CT images by projecting the 3D landmarks to 2D. The projected landmarks near the contour were moved automatically on the contour to two-dimensional anatomical locations. The landmarks in

study III were also set manually with help of 2D active appearance model for a random subset of projections to evaluate the difference between the manually and automatically set locations. The effect of altering the method of landmark setting on the estimated rotation was not significant.

6.3 TEMPLATES

6.3.1 Average templates

Several bone templates were created during these studies. In study I, two 2D images on the coronal plane called offset and depth images were used to describe the 3D shape of the proximal femur. The intensity in the offset image represented the distance from a coronal plane to the posterior surface of the femur, and the intensity in the depth image represented the thickness of the femur in the anterior-posterior direction. The average shape of the femurs in the training set was calculated by first removing the similarity transformations between the 2D landmarks of the femurs with generalized Procrustes analysis (GPA) and then by averaging the location of each landmark. The average template was then created by warping each offset and depth image to the average shape with thin-plate splines (TPS) and thereafter by averaging the intensities between the images. This template described only the average shape of the femurs.

The template in study II was created similarly as in study I except that GPA and TPS were used in 3D. This means that the average locations of the landmarks were calculated in 3D. Thereafter, each 3D CT image was deformed to the mean shape with TPS and the average BMD value between the femurs was calculated for each voxel. Therefore, the template in study II described both average shape and average 3D bone mineral density distribution for the femurs.

6.3.2 SAM templates

In addition to the average shape, SAM also describes the variation of the shape and internal density of the object. In study III, both 3D and 2D SAMs were created. In 3D, the average shape of the femurs

was first created similarly as in study II. Then an average mesh with roughly 100 000 nodes and 600 000 tetrahedral elements was created with iso2mesh open source software [194]. The mesh was warped to the shape of each femur and a vBMD value for each element was extracted from its 27-neighborhood in the CT image. Thereafter, the SAM was constructed as described in section 4.5. The SAM of the pelvis in study V was created similarly as the femoral SAM in study III.

Since in study V the FE models were created based on the femoral SAM, there were high demands on its mesh quality. Therefore, it was created with Hypermesh (11.0, Altair Engineering, Inc., Troy, USA) mesh generation software with high quality four node tetrahedral elements (283 000 nodes, 1 637 000 elements, maximum edge length of 1.5 mm). Thereafter, the mesh was deformed to the shape of each femur in the training set and the vBMD values were captured for the elements with numerical integration of the vBMD field using Bonemat software [117,195]. Subsequently, the SAM was built (section 4.5).

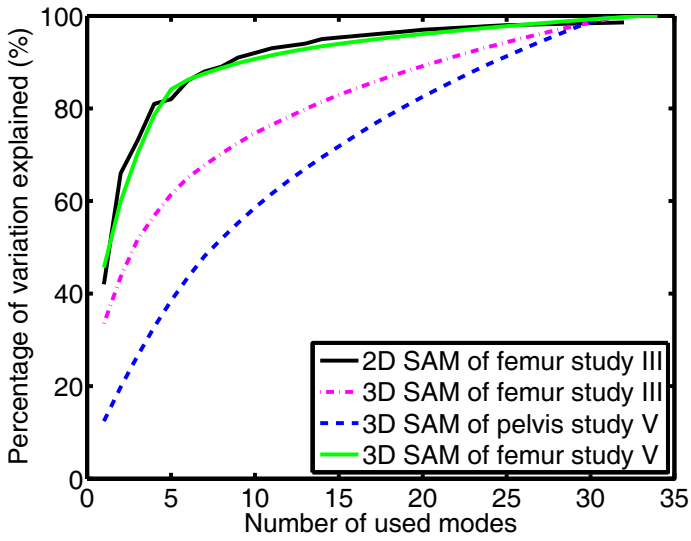

Figure 6.2: Percentage of the variation explained as a function of number of used modes for different SAMs which were used in the studies.

The compactness of the SAMs varied between the models (Fig-

ure 6.2). The two-dimensional femoral SAM from study III and the 3D femoral SAM in study V were the most compact ones, *i.e.*, the least number of modes were needed to explain a certain percentage of the total variation of the shape. On the other hand, the SAM of the pelvis was the least compact one. The SAM of the pelvis was built based on the CT images from the clinical subjects. Therefore, the radiation dose had to be smaller than with cadaver femurs. This decreased the signal-to-noise ratio in the texture of the pelvis images, which most likely had an effect on the SAM by decreasing its compactness.

6.4 RECONSTRUCTION OF 3D SHAPE FROM 2D IMAGE

The main aim of this thesis was to develop methods which can reconstruct the 3D shape and internal density distribution of a proximal femur based on a 2D image, *i.e.*, to perform a 2D-to-3D reconstruction. All developed reconstruction methods included a step where a digitally reconstructed radiograph (DRR) created from the 3D template of the femur was equalized with the base 2D image referred to as the reference image.

6.4.1 Digitally reconstructed radiograph

The DRR was created differently for a 3D image, such as a CT image or a voxel-based template, than for a mesh. For a 3D image, the DRR was created by scaling the intensity in each voxel to BMC and then by projecting the template in the anterior-posterior direction by tracing magnification-free rays which went through the 3D image. Therefore, for a 3D image $\mathbf{I}$ presented in DICOM coordinate system, the BMC of DRR in position $\mathbf{q} = (q_1, q_2)$ is

$$\mathrm{DRR}(\mathbf{q}) = \sum_{i=1}^{n} \mathbf{I}(q_1, i, q_2) \tag{6.1}$$

where n is the number of voxels in the anterior-posterior direction. Thereafter, DRR can be scaled to areal BMD.

In study V, the template was mesh-based since it was created by sampling a femoral SAM. The DRR was created from the mesh by first converting the mesh to a 3D image. A 3D image, which

enclosed the mesh, was created and the voxels which enclosed a node or the center of an element were determined. Intensity values for the determined voxels were mapped from the corresponding element centers or from their nodes. Since the resulting image was sparse, the gaps were filled with image closing operation using a properly-sized mask during the operation. The intensity values for these new object voxels were copied from their closest voxel with an intensity value. Thereafter, the DRR was calculated with equation (6.1).

6.4.2 Reconstruction of the 3D femoral shape and internal density from 2D reference image

In studies I-II the estimation, or reconstruction, was done by placing the 2D landmarks on the 2D reference image. Thereafter, the femoral average template was deformed to the shape of the reference image with TPS. Subsequently, the internal vBMD of the template was normalized such that the areal BMDs of the DRR created from the template and the BMD of the reference image agreed in each pixel.

In study V, the 3D shape was reconstructed by registering the SAMs of the femur and pelvis simultaneously to the reference image of the clinical subject. The optimal translations, rotations, scale and mode values of the SAMs were found by minimizing the sum of the absolute difference (SAD) between the DRR of the SAMs and the reference image. In a reference image of the hip, the acetabulum partly overlaps with the femoral head. Therefore, SAM of the pelvis was included. If this overlapping is not treated correctly during the registration, then the reconstruction results in too high BMD values in the femoral head. During reconstruction, the genetic algorithm in Matlab, which was used as the optimization algorithm, created a population of instances from the SAMs (Figure 4 in the original study V). Then the DRRs were created from the instances and a cost function was calculated between the DRR and the reference image. The cost function was the sum of three parts: SAD, mesh quality and anatomical position.

During reconstruction and creation of DRR, the 17 most significant modes of the femoral SAM and the 5 ones of the SAM of pelvis were varied to fit the models to the DXA image. For the femoral

SAM 95 % of the variation was explained by 17 modes and for the SAM of the pelvis 5 modes explained 37 % of the variation (Figure 6.2). Seventeen most significant mode values were used in the femoral SAM since this number was found to be sufficient for the reconstruction method in an initial test with cadaver femurs. The SAM of pelvis was only used to take into account the overlaying bones in the DXA image. Therefore, the reconstruction of the femur should be the main focus and the pelvis should reserve only a few parameters in the reconstruction process. Hence, only the first 5 modes were used since based on visual evaluation they were able to describe the main alteration in the shape of the pelvis.

The SAD was calculated at the region Ω which covered the acetabulum, the distal part of the pelvis and the proximal femur. The cost was defined as the value of SAD in g/cm^2 divided by the number of pixels covered by the bones in the region Ω.

The mesh quality was defined with the scaled minimum solid angle ($\alpha_{\min}$) [157] (section 4.9). It was calculated using the implementation in the iso2mesh toolbox [194]. The cost was defined as percentage of the elements with $\alpha_{\min}$ lower than 0.5.

In order to maximize the accuracy of the registration at the region of the hip joint, three landmarks were set to the joint space of the hip in the reference image. The distance from these points to the contour of the femoral head in the DRR was calculated. In addition, an arch of a circle was set on these three landmarks in the joint space and the distances from the arch to the landmarks 1, 2 and 6 of the SAM of the pelvis were calculated along the coronal plane. One additional landmark was set to the tip of the minor trochanter in the reference image and the distance between this landmark and landmark 4 in the femoral SAM was calculated after landmark 4 was projected onto the contour of the DRR. The cost of the anatomical position was the sum of these distances in millimeters diminished by one and scaled by 0.05. Diminishing one millimeter from the distances allowed some tolerance in the position and scaling normalized this cost to the same scale with other costs.

6.4.3 Evaluation of the reconstruction accuracy

In studies I and II, the shape was reconstructed by deforming the template to the shape of the projection obtained from the CT image.

The 18 proximal femurs were divided into training and test sets, nine bones each, and the template was created based on the training femurs. In study I, the effect on reconstruction was evaluated when the number of bones used for the template was varied from one to nine. Study II included two test cases. In the first test case, the effect of the reconstruction method itself was evaluated by using solely the CT image of the estimated bone to construct the training set. In the second test case, the template was created based on the nine training bones and the reconstruction was evaluated with the nine test bones. In study II, the reconstruction was also performed using the DXA images of the femurs in the test set, *i.e.*, DXA images of the femurs were used as reference images.

In study V, the femoral SAM was constructed using 34 proximal cadaver femurs (three femurs were excluded from the set since their shafts were too short for SAM). The SAM of the pelvis was constructed using 32 CT image sets of the pelvises of clinical subjects. The reconstruction accuracy was evaluated with a test set, which included DXA images of the hips of 13 clinical subjects. However, in order to see how the errors in the estimation accumulated during reconstruction, the method was also evaluated with the cadaver proximal femur using the leave-one-out test. In this test, one SAM was built for each set of 33 cadaver femurs and the projections of the CT images and the DXA images served as reference image.

The reconstruction accuracy was evaluated by comparing the reconstructed femoral shape with the shape from the CT image of the same femur. Therefore, the reconstructed shape and the CT images were superimposed with the ICP algorithm. In studies I, II and V, the volumetric difference between the shapes and the mean and maximum point-to-surface distances between the surfaces of the CT image and reconstruction were calculated. These parameters were calculated at the region of whole femur and at different parts of the femur, *i.e.*, at the head, neck, trochanter and shaft. In study I, the reconstructed BMD inside the femur varied in the coronal plane but was constant in the anterior-posterior direction. On the contrary, the BMD distribution was reconstructed in 3D in studies II and V. Therefore, in these studies, the average difference in the vBMD reconstruction was calculated for the whole proximal femur and for each sub-region. In study II, the difference was calculated by

computing the mean of the voxel-by-voxel absolute differences. In study V, the vBMDs were compared element-by-element between the isotopological reconstructed mesh and the mesh that was directly warped to the shape of the test femur.

6.5 MECHANICAL SIMULATION OF PROXIMAL FEMUR

The effect of the 2D-to-3D reconstruction errors on the mechanics of the femur was evaluated. Linear elastic FE models with isotropic material properties were created based on the reconstructed shapes. Their stiffness, strains and stresses were compared with those from the FE models created using the CT image of same femurs. A load equal to force during the stance phase was directed on the femoral head [196]. In studies I and II, the load was 2.25 times the body weight. The force was directed to femoral head 12.5° medial from the shaft axis direction. In study V, the load was 1.5 times body weight and 10° [197] medial from shaft axis. The movement of the nodes at the distal shaft were constrained in all directions. In studies I and II, the mesh was created by meshing the voxel-based reconstructed images and CT images with about 65000 elements and 15000 nodes with iso2mesh open source meshing software [194] in Matlab. In study V, the SAM created isotopological FE meshes automatically. The same isotopological mesh was also warped to the shape of each test femur, and these meshes were used as the reference FE model. Isotopogical mesh means that each node in all meshes is located in the same anatomical location. Around 283000 nodes and 1600000 elements were used in the mesh. In study V modal assurance criterion (MAC) was calculated between the reference and reconstruction-based FE models in addition to other parameters.

In study V, the element quality was globally good in all automatically generated patient-specific isotopological meshes. However, in some meshes a few elements (4 ± 6, median 0, maximum 29) were distorted, which led to zero-volume elements. FE solvers cannot handle these elements. Therefore, an automatic Matlab algorithm was iteratively used to enhance their quality:

1. The algorithm called Ansys to import the mesh and to determine excessively distorted elements (using the CHECK com-

mand)

2. If zero-volume elements were detected, one of the nodes was moved by a distance equal to 1/3 of its distance to the nearest adjacent node not belonging to the treated element. The node to be moved and its direction were defined according to:
   (a) If two coincident nodes were found, one of the two was moved towards the direction normal to the largest element face of the adjacent elements
   (b) If one node was lying on the face of the element formed by the other 3 nodes, the node was moved along the negative normal of that face

6.6 ROTATION OF FEMUR IN 2D RADIOGRAPHS

The orientation of a femur in a 2D radiograph is an essential information both in clinical diagnostics and for 2D-to-3D reconstruction methods. In clinics, the misalignment of femur may lead to incorrect interpretation of the radiographs. On the other hand, a 2D-to-3D reconstruction method which does not take account of the 3D orientation internally requires external estimation of the orientation. Therefore, in study III, a method that estimates the 3D orientation of a femur in a 2D image was developed. In the method, the shape and intensity of the femur in a 2D image was parametrized with 2D SAM and the relation between the parameters and known rotations in the training set was described with a linear regression or ANN. A benefit in ANN, compared to a linear regression, is that it is able to utilize also non-linear relations in the regression. To build a training set that is large enough for ANN, a 3D SAM was constructed from 33 cadaveric femurs. Then the SAM was sampled 500 times by varying the ten first modes randomly between ± 2 SD to produce 500 artificial femurs. Variation of the mode values was limited to ± 2 SD since growing the variation range over ± 2 SD lead to rough surface on the sample bones. This indicated that the shape was not any more realistic. Ten first modes explained 75 % of the total variation of the model (Figure 6.2). It was decided that this number of modes were enough since it resulted to sufficient alteration in the bone shapes. The test set included 19 femurs, which were segmented from clinical CT images.

Both the artificial femurs in the training set and the femurs in the test set were rotated in three different directions and a DRR was created in each orientation:

1. $\pm 20^\circ$ with 2° division around the shaft axis (internal/external rotation).
2. $\pm 10^\circ$ with 2° division around the medial-lateral axis (flexion/extension of hip).
3. by simultaneous rotation around both axes, *i.e.* $\pm 16^\circ$ with 4° division around the shaft axis and $\pm 8^\circ$ with 4° division around the medial-lateral axis.

A DRR set with internal/external rotation (rotation type 1) was created also for the original proximal femurs in the training set.

The 2D SAMs in study III were built by using an active shape model toolkit (Manchester University, Manchester, UK) [135, 138]. For each rotation type, one 2D SAM was created based on the artificial femurs. Thirty first modes, which explained 98 % of the variation in the set, were extracted for each DDR in the training set. A fourth statistical 2D SAM was build based on the DRR set of the original proximal femurs. The four 2D SAMs were registered to DRRs of the corresponding test set and the mode values were extracted also for them.

The effect of rotation on mode values of the 2D statistical shape and appearance models were evaluated with the help of the original training femurs. The 3D femurs were rotated around shaft axes in $\pm 10^\circ$ with 2° division and DRRs were created. The 2D landmarks of the projections were set based on 3D landmarks. Then the 2D active shape and appearance models were created with Cootes software and mode values for each projection were extracted. The effect of rotation in each mode was evaluated by comparing the standard deviation of the mode value due to rotation (mean of standard deviations of each bone due to rotation) against total variance of the mode value.

A linear regression model was trained with the mode values of the SAM of the original proximal femurs and with the corresponding known rotations. To avoid over fitting, an optimal number of coefficients for the linear regression was found with the leave-one-out test by adding modes with the highest correlation to the model

as long as the accuracy of the estimation increased and maximum was found. As a result, the 16 the most significant modes that explained 96 % of the total variation of the 2D SAM were used in the linear regression model.

Three different ANNs were trained with the mode values from the three SAMs of the artificial femurs and with known rotation angles. The least varying modes had no significant effect on the prediction accuracy of the rotation. Therefore, it was decided that all 30 modes were used with the ANN. The structure of the used ANNs was multi-layer perceptor (MLP) with 40 nodes and two hidden layers, which showed good performance in a preliminary test. Finally, the linear regression and the ANNs were used to predict the rotations in the DRRs of the test sets.

6.7 MECHANICAL TESTING AND MEASUREMENT OF SURFACE STRAINS ON COMPOSITE FEMUR

In study IV, six composite femurs were cut 150 mm below the minor trochanter and the distal shafts were aligned vertically and embedded to epoxy in depth of 50 mm. The anterior surfaces were sprayed for DIC with white background and then with black speckle pattern. Lastly, the bones were imaged with a CT scanner (Table 6.3).

The bones were mechanically tested under axial compression (Figure 6.3). The distal shafts were constrained with a clamp. The load was measured with a load cell (20 kN Zwick, accuracy ± 0.27 %) from the femoral head, while the table where the distal shaft was attached moved upward with a constant displacement rate of 1.0 mm/min (± 0.15 %). The displacement of the table and the load from the load cell were recorded.

During mechanical testing, two cameras (4 MPixels, Limess, Krefeld, Germany) with a frame rate of 4 Hz recorded the anterior surface of the composite femurs. The 3D surfaces, local displacements and strains were calculated from the stereo view of the cameras using DIC software VIC-3D 2007 (Correlated Solutions, Inc., USA).

The 3D surfaces were reconstructed from DIC data and were registered with iterative closest point algorithm written in Matlab to the orientation of the initial CT image of the corresponding

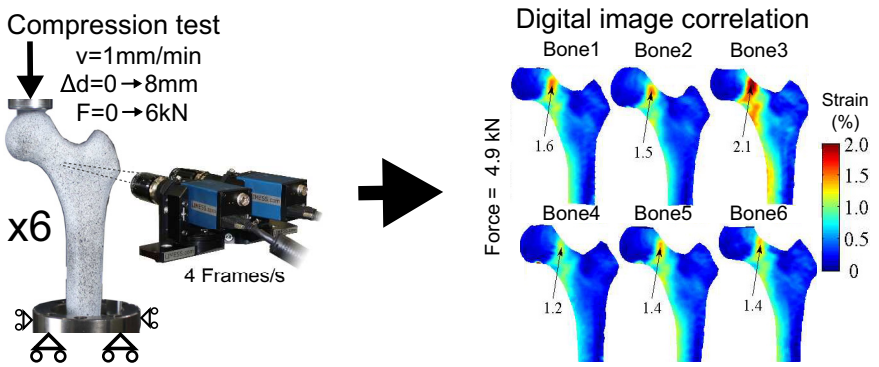

Figure 6.3: Six composite femurs were tested under axial compression until fracture. The anterior surface was recorded with two cameras for DIC. Pan angle of the middle point between the cameras was $22^\circ \pm 2.2^\circ$ towards medial from the anterior view. The surface displacements and strains were calculated from the DIC data.

composite femur. The accuracy of the surface reconstruction was evaluated. The first and second principal strains were analyzed one frame before fracture. To evaluate the inter-sample variation, the von Mises strains were plotted and evaluated for those frames where all bones were under equal load of 4.9 kN and where all bones were under an equal maximum von Mises strain of 1.7 %. The local von Mises strains were investigated against force in the head-neck junction, *i.e.*, site for the highest strains. The noise in the DIC data was analyzed. The initial CT images of the composite femurs were co-registered with Analyze software (Analyze 10.0, Analyze direct, Inc., KS, USA).

6.8 STATISTICAL ANALYSES

The limit of statistical significance in all statistical tests was set to $p < 0.05$.

In study I, Kruskal-Wallis test in SPSS software (v. 14.0, SPSS Inc., Chicago, IL, USA) was used to evaluate whether the reconstruction accuracy of the femoral shape was dependent on the number of femurs in the training set.

In studies I, II and V, linear Pearson's correlation tests between the stresses and strains of the FE models were calculated with Matlab (v. 7.6, Mathworks, Inc., Natick, MA)

In study III, the significance of the difference between the estimation accuracy of the rotation of the linear regression model and ANN was tested using the paired Wilcoxon signed rank test (Matlab).

7 Results

7.1 RECONSTRUCTION OF FEMORAL SHAPE AND INTERNAL DENSITY FROM 2D REFERENCE IMAGE

The reconstruction accuracy of the shape of the cadaver proximal femurs for the methods in studies I, II and V is presented in Figure 7.1. The accumulation of the mean surface difference in study V is presented in Figure 7.2. The reconstruction accuracy of the 3D vBMD (studies II and V) is presented in table 7.1. As shown in Figure 7.3, the methods used in studies II and V could both reconstruct the 3D density distribution of the femur and distinguish the main parts of the femur such as the cortical and trabecular bone.

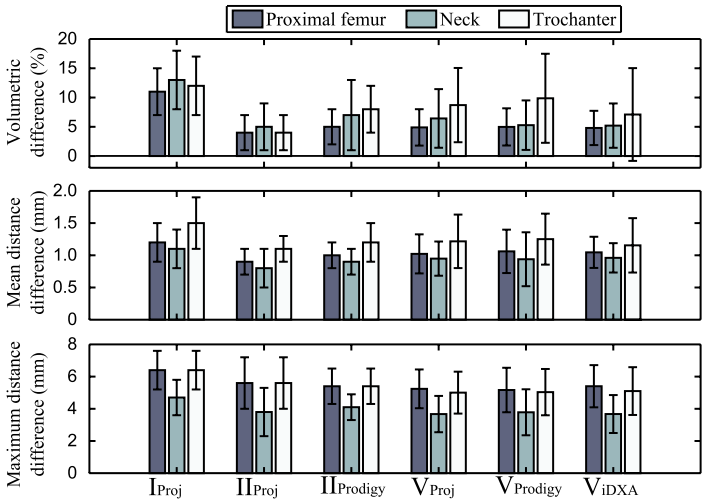

Figure 7.1: Mean volumetric difference, and mean and maximum distance difference between the reconstructed shape of the proximal cadaver femur and the original shape from a CT image in the region of the whole proximal femur, neck and trochanter. The shape was estimated using the methods presented in study I, II and V. Projection of the CT image (Proj), or DXA image from Prodigy or iDXA instrument was used as the reference image in the reconstruction. The difference in the accuracy between the methods in studies II and V and the effect of different reference images were minor.

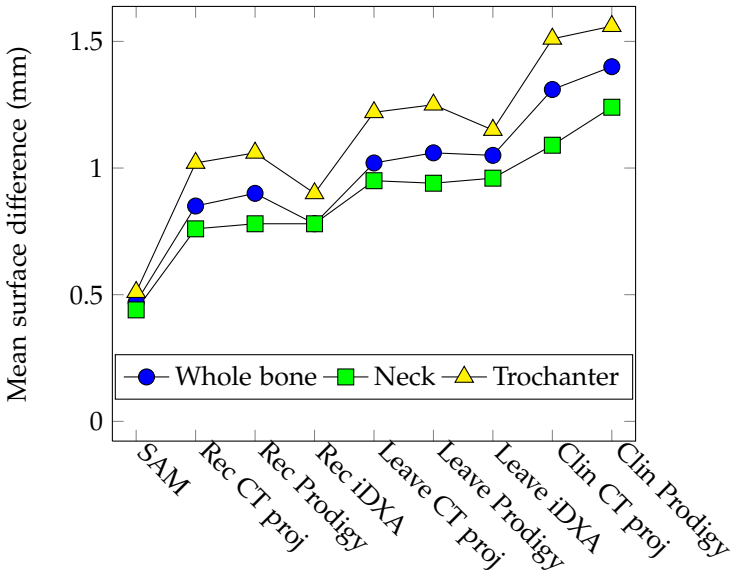

Figure 7.2: Accumulation of the mean surface difference between the original CT image and estimated shape at different regions of the femur. Accumulation of the mean surface difference were evaluated as follows: First the correct (truncated) mode values were given for the SAM (SAM), then the cadaver proximal femurs were reconstructed by recreating them such that the training set of the SAM included the tested femur (Rec). Subsequently the leave-one-out examination was done by excluding the tested bone from the test set (Leave). Lastly, the reference images of the clinical subjects, where both pelvis and femur were included, served as the test set (Clin). Projected CT or DXA image from Prodigy or iDXA scanner was used as the reference image.

Table 7.1: Difference in the vBMD between the reconstructed shape of the proximal cadaver femurs and original QCT in the region of the whole bone, neck and trochanter (mean ± SD). The shape and vBMD was estimated using the method in study II or V. The projection of the CT image or DXA image from Prodigy or iDXA scanner was used as a reference image in the estimation.

Study	**Reference image**	**Difference in vBMD (mg/cm^3)** Wholebone	Neck	Trochanter
II	Proj	120 ± 8	124 ± 6	131 ± 10
	Prodigy	140 ± 11	163 ± 21	161 ± 14
V	Proj	176 ± 77	132 ± 18	194 ± 122
	Prodigy	178 ± 77	132 ± 20	189 ± 114
	iDXA	210 ± 86	127 ± 18	182 ± 98

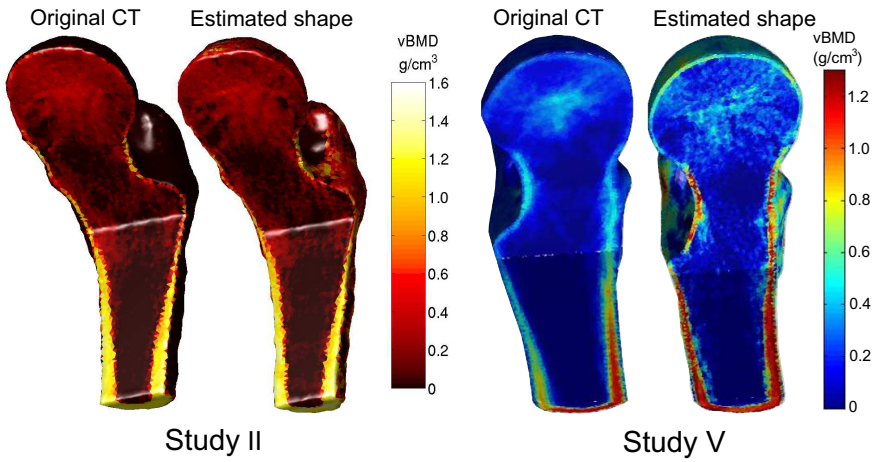

Figure 7.3: Representative examples of the estimated shapes and vBMDs using methods in study II and V. Both methods were able to estimate the vBMD in all three directions and were able to distinguish the trabecular and cortical bone. In study II, the shape was reconstructed based on the projected CT whereas in study V the shape was reconstructed using a DXA image of the hip of a postmenopausal woman. The method over estimated the BMD values since the training set consisted of middle-aged males with higher BMD values than that of the test subject.

7.2 MECHANICAL CHARACTERISTICS OF RECONSTRUCTED FEMUR

The stiffness, which was defined as the ratio between the load on the femoral head and the displacement of the head, was compared between CT-based models and models built based on the reconstructed shape, with the projection of the CT image as a reference image:

- In work I, the difference in stiffness was $31 \pm 25\,\%$, $r^2 = 0.83$
- In work II, the difference in stiffness was $-7 \pm 16\,\%$, $r^2 = 0.83$
- In work V, the difference in stiffness was $3 \pm 18\,\%$, $r^2 = 0.78$

When the FE analysis was based on clinical DXA images, a linear regression between the stiffnesses of CT-based and DXA-based FE models was $y = 1.36x + 54.5$ with correlation $R^2 = 0.85$ (Figure 7.4).

The MAC value between the reconstruction-based and CT-based FE models in study V was 0.978 ± 0.016 when projected CT was

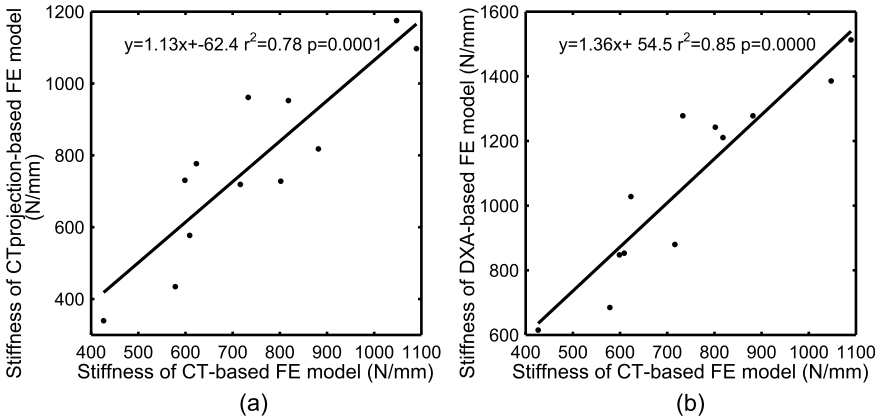

Figure 7.4: (a) Stiffness between CT projection-based and CT-based FE models and (b) stiffness between DXA-based and CT-based FE models. Evaluation was done with CT images and DXA images of clinical subjects (set F)

used as reference image and 0.977 ± 0.019 when DXA image from Prodigy was used as reference image.

7.3 ESTIMATION OF ROTATION IN FEMORAL 2D IMAGE

The effect of rotation on the mode values is presented in Figure 7.5. All modes of both the statistical shape and the appearance models were affected by rotation but none of the modes were fully explained by the rotation. The first three modes in the shape and appearance models were equally related to rotation. The fourth mode was the first mode that differed between the models with regards to the rotation. The results suggest that the appearance model is more affected by rotation than the shape model.

Sixteen modes were included in the linear regression-based predictive model. The used modes were chosen based on the correlation between the modes and the rotations. The number of used modes was based on the prediction accuracy of the rotations as a function of number of modes evaluated with leave-one-out test. The linear regression predicted the rotation around the shaft axis with an accuracy of $4.6 \pm 3.4^\circ$ when the method was trained with cadaver femurs and tested with leave-one-out test. The accuracy was $4.9 \pm 5.2^\circ$ when the method was trained with artificial femurs and

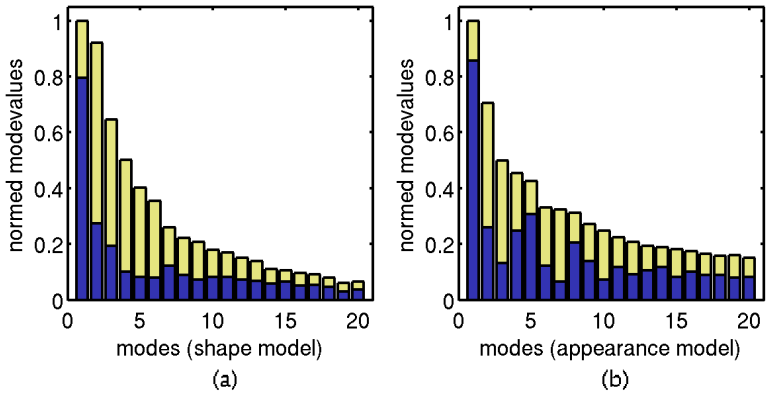

Figure 7.5: Amount of rotation in the 20 first modes of the 2D statistical shape model (a) and the 2D SAM (b) created from DRRs of CT images of cadaver proximal femurs and femurs of clinical subjects (total of 52 images). Blue bars describe mode variation (SD) related to rotation, yellow is the variation not related to rotation and sum of yellow and blue bars describe total variation of the modes. The DRRs were created after the femurs were rotated around shaft axis (medial/lateral rotation) between $\pm 10^{\circ}$ and with division of 2°.

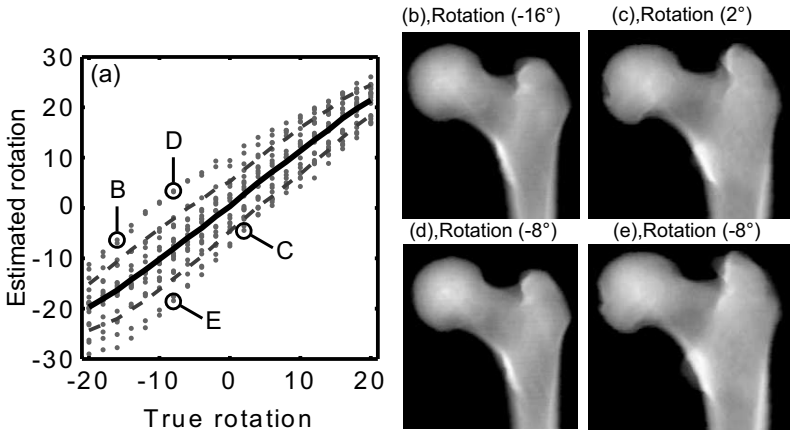

Figure 7.6: Four bone projections derived from estimation of rotation where ANN was trained with artificial femurs and prediction was tested with clinical femurs. Images B D, and C E are projected from the same bones with different rotations. Images B and C, had same estimated rotation, and D and E had same true rotation. In images B and C, the neck length, size of the contour of the minor trochanter and distance from neck-trochanter boundary to the most lateral point are nearly equal. In images D and E these measures differ extensively. Reprinted from Publication Journal of Biomechanics, Vol 45, Väänänen, S. P., Isaksson, H., Waarsing, E., Zadpoor, A. A., Jurvelin, J. S., & Weinans, H., Estimation of 3D rotation of femur in 2D hip radiographs, pp. 2279-2283, Copyright (2012), with permission from Elsevier.

tested with clinical femur (Figure 3 in study III). When the ANN was trained with artificial femurs and tested with clinical femurs, the accuracy of the prediction was $4.0 \pm 3.4^\circ$ (Figure 7.6). Hence, ANN was more accurate than linear regression ($p = 0.018$). ANN predicted the rotation around the medial-lateral axis with mean absolute error of $2.2 \pm 1.5^\circ$ and both rotation simultaneously with accuracies of $2.4 \pm 2.0^\circ$ and $4.9 \pm 4.1^\circ$.

7.4 SURFACE STRAINS IN COMPOSITE FEMUR

All fractures of the composite femurs during mechanical testing were instant cracks. Therefore DIC with 4 Hz frame rate was not able to capture images during the ongoing fracture process. The fractures were located at the neck-trochanter junction except in one bone, which fractured below minor trochanter. An air cavity located in the lateral cortex next to the neck axis was the most probable cause for this atypical fracture pattern. The shape of the femurs and the thickness of the cortex were highly similar between all femurs (supplementary Figure 1 in the study IV). In most regions these differences were in the same order of magnitude as the voxel size in the CT images.

The load-displacement curves agreed well between the bones in the linear region except in bone 4, which was clearly stiffer than the other bones (Figure 7.7). The fracture load varied between 4954 and 6747 N among the bones. The yield properties of bone 2 differed from those of the other femurs, since its ductility after reaching the yield point was higher than in the other bones. This higher ductility is also present in the measured strains since the other bones fractured when the maximum von Mises strain reached 2 % (Figure 7.7) whereas bone 2 reached Von Mises strain of 4 % before it fractured.

It seems that the local temporal disturbance in the DIC data was due to the curvature of the surface, and not related to the

[1]Reprinted from Publication Journal of Biomechanics, Vol 46, Väänänen, S. P., Amin Yavari, S., Weinans, H., Zadpoor, A. A., Jurvelin, J. S., & Isaksson, H., Repeatability of digital image correlation for measurement of surface strains in composite long bones, pp. 1928-1932, Copyright (2013), with permission from Elsevier.

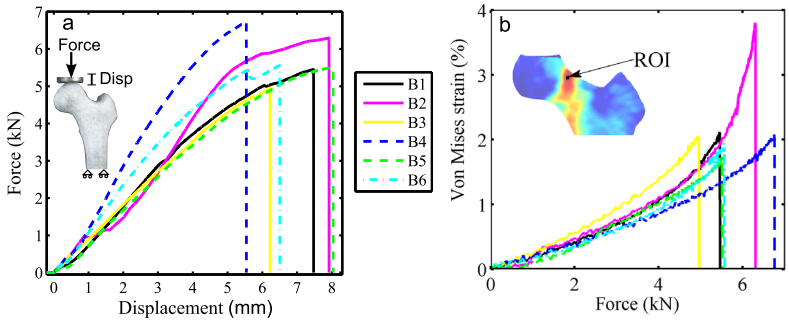

Figure 7.7: (a): Load-displacement curves under axial compression for all six composite bones (B1-B6). The variation in the fracture load and the slopes of the linear region were 11 % and 26 %, respectively. (b): the von Mises strains within the ROI at the head-neck junction where the strains were highest as a function of force for all bones. Five bones reached 2 % strain before fracture. The bone 2 was able to bear almost two times higher strains before fracture. Furthermore, its strain-versus-force response was nonlinear at high strains.[1]

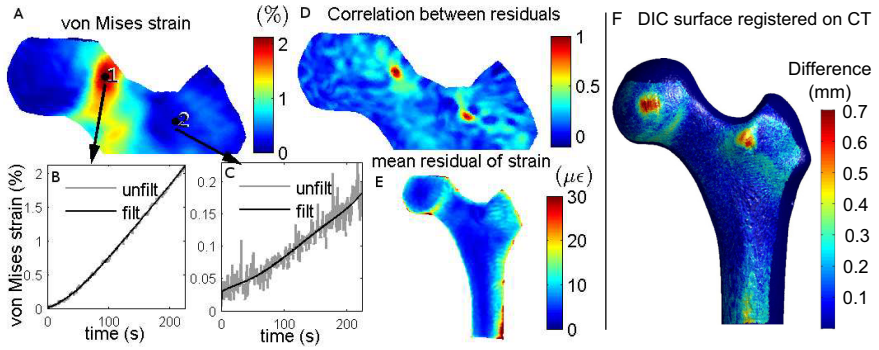

Figure 7.8: DIC data and its temporal disturbance in a representative femur. (A): The location of two points 1 and 2. B shows original DIC data and C shows data filtered by fitting a fifth order polynomial on the signal at the points 1 and 2, respectively. Residual at each location was calculated by subtracting the fitted curve from the original DIC data. (D): shows the result when the residuals of points 1 and 2 were correlated with all other points. Residuals of points near each other were highly correlated. E shows the RMS value of the residual. Largest RMS values were found from regions where the angle between the surface and the image plane in DIC was high. (F): Average registration error between the DIC surface and the CT image surface. The registration error was less than 0.4 mm at the weight bearing regions. The registration was least accurate at the most anterior points of the head and major trochanter.[1]

strain levels. The disturbance in the data increased with increasing angle between the DIC surface and the image plane (Figure 7.8). On the surfaces parallel to the imaging plane, the disturbance was around 5 $\mu\epsilon$ whereas on regions with a large angle, the disturbance increased to 30 $\mu\epsilon$. Auto-correlations calculated from the temporal disturbance indicated that the temporal disturbance was noise since it was memory-free. The surface reconstructed with DIC agreed well with the surface captured with CT (Figure 7.8). The average difference between the surfaces was less than 0.4 mm in most regions. The largest differences were found at the most anterior location of the head and trochanter.

The highest first principal strains, *i.e.*, tensile strains, and von Mises strains were found at the superior head-neck junction (supplementary Figure 2 in study IV) and the lowest second principal strains, *i.e.*, the compressive strains were located in the inferior neck region. When all bones were loaded with equal force, the inter-bone variation of the von Mises strain at the region of high strains was 20-25 % both in the linear range and near fracture (Figure 4 in the original publication). In the case of equal maximum strain, the variation in the other regions were 5-10 %. When the strain value decreased below a threshold value 0.3 %, the variation of strain increased over 40 % in both cases.

8 Discussion

The aim of this thesis was to develop methods that could improve the diagnostics of osteoporosis and the prediction of fracture risk, based on the current gold standard method DXA imaging. Therefore, in studies I, II and V, methods were developed that can reconstruct the 3D shape and internal density of the proximal femur with the aid of single 2D image. Then, an FE model which calculates the mechanical characteristics of the femur was created based on the reconstructed bone shapes. The femoral strength estimated based on a DXA image includes the contributions of the femoral geometry, structure and density. Therefore, it has a good potential to improve the prediction of the fracture risk of a patient compared with prediction based on BMD measured with DXA.

Studies III and IV support the developed methods in the three other studies. In study III, a method that could estimate the 3D orientation of the femur in a 2D image was developed. This method is necessary if the 2D-to-3D reconstruction methods developed in studies I and II are to be used for clinical DXA images since they do not account for the possible misalignment of the femur during imaging. In study IV, strain distributions on the anterior surface of composite femurs were measured with the DIC technique during a destructive mechanical test. The measurement of strains with DIC can provide important validation data for DXA-based FE models for future studies.

8.1 RECONSTRUCTION TECHNIQUES OF FEMORAL SHAPE FROM 2D REFERENCE IMAGE

In studies I, II and V, three different methods were developed to reconstruct the 3D surface of the proximal femur from one 2D reference image in order to create patient-specific FE models based on the reconstructed shapes. Projected CT images or DXA images were used as the reference images. Studies I and II utilized an average template which described the average shape of the proximal femur in the training set. The template was warped to the shape of a ref-

erence image by aligning anatomical two-dimensional features, *i.e.*, landmarks, between the template and the reference image. Since the template in study I was constructed from two 2D images, the offset and depth images, it included no information about the 3D density distribution. On the other hand, the template in study II was constructed fully in 3D; therefore it was able to estimate the BMD distribution in all three directions. In study V, the template was based on a SAM, so for this reason it included prior information about both the average shape and density distribution of the proximal femur and their variation within the population. The genetic algorithm was used in study V to register the template to the reference image by minimizing the difference between the reference image and projection of the template. Consequently, the methods in study V should intuitively reconstruct non-regular 3D shapes more accurately than the other two methods.

In studies II and V the shapes of the proximal cadaver femurs were reconstructed with similar accuracy (point-to-surface distance 1.0 mm), and they were more accurate than the method used in study I (Figure 7.1). Thus, methods based on a 3D template are superior to methods where several 2D images are used as the template to reconstruct the 3D surface. An advantage of the method introduced in study I is that it is computationally much lighter than the other methods since only 2D deformations are needed during the reconstruction. The accuracy of the DXA image-based reconstruction of the femurs of clinical subjects was 1.4 mm. In the cadaver femurs, used to compare the methods used in studies II and V, diseases that may affect bone metabolism were excluded. This most likely excluded also pathological bone shapes, and this fact account for the similar accuracy between general template-based and SAM-based reconstruction methods.

The results in the literature regarding different femoral shape reconstruction techniques are not always directly comparable with each other. In most studies, the reconstructed shape is compared with the true shape obtained from CT or MRI images. However, since the imaging resolution varies and different training and test sets are used, the accuracy is affected as well. Most authors report the mean point-to-surface distance between the reconstructed shape and the true CT images, whereas some provide details only

about the similarity between the reconstructed and true 3D shape parameters [181, 186]. When only one DXA or X-ray image is used for the reconstruction, the mean point-to-surface distance varies between 1.1 and 3.0 mm in literature [36, 38, 40, 184, 198]. Thus, the current findings are among the most accurate presented in the literature. In general, SAM-based methods [182, 184, 198] seem to achieve more accurate reconstruction than general template-based methods [36, 38, 40], even though the methods in this thesis showed similar accuracy.

All methods reconstructed the 3D shape more accurately in the more symmetrical areas such as at the head and neck than in the irregular areas, *e.g.*, at the trochanter. This finding has been confirmed in other studies [38, 182]. It supports the usage of shape reconstruction methods since the neck and head areas are the most important for fracture prediction. In fact, the trochanteric fractures are more strongly related to BMD of the femur than the cervical fractures [90]. Therefore, BMD measured with DXA may detect increased trochanteric fracture risk, whereas cervical fractures are strongly dependent on geometry and thus their risk could best be identified with DXA-based FE models.

Compared with projected CT images, DXA images have a lower signal-to-noise ratio. In addition, DXA images from the Prodigy scanner have much lower resolution than the images from the iDXA scanner. However, an unanticipated finding was that changing the reference image had only a very minor effect on the reconstruction accuracy (Figure 7.1 and Figure 7.2). Clearly, all reference images used contained enough information about the 2D shape for reconstruction. In that respect, other sources of errors, such as the lack of information in the third direction, were dominant. The results suggest (Figure 7.2) that the SAM creation, re-creation of the shape through 2D-to-3D reconstruction, and a non-optimal training set are the major sources of error. The training set of the SAM was more optimal for the leave-one-out test than for the test set of clinical subjects. This was because the training set consisted of the proximal femurs of middle-aged males but the latter test set included the femurs of postmenopausal women. Therefore, the results of the latter test represent the extreme limits for the reconstruction error. Presumably, the accuracy will increase when a more optimal

training set is used for postmenopausal women.

The methods in studies II and V were able to distinguish the main features in the femur such as the cortical and trabecular bone. The differences between the estimated and true vBMDs were moderate (140-210 mg/cm^3). Only Whitmarsh and co-authors [182, 198] have reported average error in the reconstruction of the vBMD voxel by voxel. Their reported reconstruction accuracy was somewhat higher than the accuracy presented in the present study (72-81 mg/cm^3). Whitmarsh evaluated the accuracy using 1 mm^3 voxels. In study II, the size of the voxels in the evaluation was $\leq$ 0.22 mm^3 which leads to a less averaged evaluation. In study V, the vBMD was evaluated element-wise, leading to even more detailed assessment since the elements were smaller than voxels in study II. A standardized method to evaluate differences in the density distribution would help in a comparison of the performance of different reconstruction techniques.

The method used in study V had the advantage that it also accounted for the possible misalignment of the femur during imaging. Misalignment should be considered since the position of the proximal femur during DXA imaging may not be constant due to varying positioning of the patient and varying anteversion angle of the femur. The anteversion angle in the normal population varies with SD over nine degrees [199]. The misalignment encountered in the femoral images can also be corrected in the method devised in study II if the orientation of the femur is first estimated using the methods presented in study III. In one of the tests the misalignment was corrected when the DXA images of the cadaver femurs were used as the reference image. However, the correction of the orientation had a little effect on the accuracy of the reconstruction. This was most likely since the cadaver femurs were well aligned during imaging.

The second advantage of the method developed in study V was that it simultaneously aligns the SAMs of the pelvis and femur and the reference image. Therefore, the method can estimate the shape and density of the femur even though the pelvis and femur overlap at the joint in the DXA images of clinical subjects. This approach was advantageous, since the head was the most accurately estimated part of femur (Figure 7.2). In other studies, the head re-

gion has been extrapolated on the basis of the shapes of the other regions of the femur and this led to the largest errors in head [182].

In the clinical setting, an automated reconstruction method of the 3D shape is useful as it does not increase the work load. In studies I and II, the method needs 27 landmarks in the reference image. Landmark positioning in studies I and II was partly automated, but some landmarks required manual adjustment when used with DXA images. The method deviced in study V was used to estimate the femoral shape and produced the FE mesh automatically. However, in an attempt to increase the accuracy in some regions, three landmarks were set manually on the joint space and an additional one to the contour of the minor trochanter. By presenting a second cost function in this region, manual landmarking may become unnecessary.

If the methods presented in studies I, II and V are used to reconstruct femoral shapes within a population, several templates are needed. Study V suggests that these methods could improve their accuracy if separate templates for different genders and ethnic groups are in use.

8.2 MECHANICAL CHARACTERISTICS OF RECONSTRUCTED FEMUR

In studies I, II and V, an FE model built using the reconstructed shape was compared with the corresponding QCT-based FE model. In study I, the Young's modulus values in the models varied in 2D whereas in studies II and V the moduli in the models varied in 3D. Correlation of the stiffness between the QCT-based and reconstruction-based models in all studies was over $r^2 = 0.78$. It was highest for DXA-based FE model in study V ($r^2 = 0.85$). This shows good agreement between the models. The MAC value between the models in study V was 0.98 which manifests an accurate match between the local displacements. Therefore the present results are encouranging and highlight the good agreement for the FE model obtained from the reconstructed shapes and the results from experimental tests. This will be verified in the future studies. In the literature, FE analysis after the 2D-to-3D reconstruction has been presented in only a few studies. Langton and co-

authors [200] reported good agreement ($r^2 = 0.804$) between the stiffness of reconstruction-based FE models and experimental failure loads. This agrees with the present findings. Galibarov and co-authors [38] showed that the error in the FE-predicted surface strains increases linearly with errors in surface reconstruction.

Since the present aim was to evaluate how the errors from the reconstruction affected the outcome of the FE modeling, the FE models included only linear isotropic material properties and a simulated stance load. Results from earlier studies have demonstrated that bone behaves highly linearly under physiological loading rates [64]. When the model is used for prediction of the fracture, yield and fracture criteria and fall-related loading conditions must be included into the model.

The benefit of patient-specific FE analysis, as compared with measurement of BMD only, is that it incorporates automatically the contributions of the patient's distinctive geometry. With FE analysis, one can directly calculate the strength of the bone and evaluate different loading or fall scenarios to identify the most fragile site of the femur. This may be useful in guiding individuals to take appropriate actions to avoid osteoporotic fractures.

8.3 ORIENTATION OF FEMUR IN 2D IMAGE

8.3.1 Amount of rotation in modes

The effect of bone rotation on the modes of femoral 2D statistical shape and appearance models was evaluated. The results showed that all modes were affected by rotation, but none of the modes were solely explained by this parameter (Figure 7.5). This fact makes the interpretation of the 2D mode values more challenging, for example, when a 2D SAM is used to analyze femoral shape or when a mode is related to a measure of diagnostic indicator of osteoarthritis, such as joint space width or Kellgren and Lawrence score [201]. The changes in the mode values may relate to different orientation or to true changes in the shape. In order to separate the variations in true shape from artificial differences related to changes in the orientation, a 3D SAM-based 2D-to-3D registration method can be used.

8.3.2 Estimation of rotation

Since no mode value itself was able to describe rotation (Figure 7.5), two predictive models were created: linear regression model and ANN. The benefit with the linear regression model is that a moderately sized training set is sufficient to train it, whereas ANN needs a large training set. A total of 300 artificial femurs were enough to produce sufficient results with ANN. However, in order to guarantee a robust convergence of the training, 500 artificial femurs were included in the final training set. A drawback with the linear regression model is that it only utilizes linear relations between the input parameters and outcome, whereas ANN also accounts for nonlinearity. This partly explains why ANN was about 20 % ($p = 0.018$) more accurate predictor of rotation than the linear regression. The mean absolute error for the prediction with ANN around the shaft axis was 4.0°. In comparison, orthopedic surgeons can estimate rotation of the femur with a mean accuracy of 12.1° (SD 7.1°) [202]. Whitmarsh and co-authors [182] reported that femoral 3D SAM which was aligned to DXA image estimated the 3D rotation around the shaft axis with accuracy of 3.0°. However, the scale of the true rotations was not reported. The true rotation was found by aligning a CT image of the evaluated femur to the DXA image, by using the same optimization and similarity measure that was used with the SAM. This may have influenced the accuracy.

Interestingly, the rotation around the medial-lateral axis (2.2°) was predicted more accurately than the rotation around the shaft axis. The same has also been reported earlier [182]. This may be explained by the shape variations in the femur. The width of the major trochanter and the size of the contour of the minor trochanter may vary greatly between two 2D projections of femurs even though the true rotation is kept constant between them (see D and E in Figure 7.6). On the contrary, even though the true rotation differs significantly between two femurs, their appearance in the projections may be very similar (Figure 7.6 B and C). In the vertical direction, the variation in shape is less dramatic which implies that the changes in the appearance are mostly due rotation.

This method has a good potential to reveal differences in the position between two bone sets, and it can also support the 2D-to-3D conversion. For example, the method could differentiate two

groups with different standing positions during X-ray imaging, *e.g.*, due to pain or some other functional limitation. It can also be useful when one wants to correct errors due to rotation in parameters derived from hip X-ray images.

8.4 SURFACE STRAINS ON PROXIMAL COMPOSITE FEMUR MEASURED WITH DIC

Experimental measurements and numerical models describing the femur mechanics have positive synergies [161]. Numerical models usually allow a faster and more cost-effective approach to evaluate different geometries and loading conditions. However, accurate experimental data is critical if one wishes to validate the models. Therefore, an experimental evaluation of bone mechanics with the relatively new technique DIC was a natural part of this thesis project. This was conducted to capture the surface strains of whole proximal femur.

In study IV, six presumably identical composite femurs were loaded axially using a constant displacement rate until fracture. The fractures occurred instantaneously regardless of the low displacement rate used in the test. The fracture patterns on the femurs were nearly identical in all bones. However, the fracture location through the neck-trochanter junction was slightly more lateral than that typically reported for human cadaver femurs subjected to an axial load [68,203].

The fracture loads in human cadaver femurs under axial load have been reported to vary between 3000 N to 13000 N [29,204]. The fracture load is clearly related to the bone quality, the loading angle and the shaft length [64]. Typically, when the shaft lengths and load angles are fixed, the fracture load varies around 30 % between different cadavers [29]. Therefore, the fracture loads for composite bones were within the variation of human cadaver bones, and, as expected, the variability of fracture loads (11 %) was smaller in composite bones than in human cadaver bones. This shows that composite bones can be more useful than cadaver bones when conducting technical repeatability analyzes.

In DIC, the thickness of the paint layer is a fraction of a millimeter and the stiffness of the paint is low in comparison with the

stiffness of the bones. Therefore, the reinforcing effect of the paint can be considered as negligible. This is a clear benefit in the DIC technique over the use of strain gauges. In fact, strain gauges have been reported to affect the strains on the femur. Depending on the measurement site, their reinforcement effect may decrease the actual strains from 1 up to 15 % [70, 205]. Another benefit is that DIC can measure the displacements and calculate the strains on the whole imaged surface. Therefore, it provides 10000-50000 independent measurements, whereas strain gauges provide only local strains in a maximum of 10-15 locations. When high-speed cameras are used, DIC can also achieve the same temporal resolution as strain gauges.

The RMS value of the disturbance in the temporal DIC signal was between 5-30 $\mu\epsilon$. The amount of disturbance was related to the angle between the DIC surface and the image plane. The DIC software in use provided no filtering in the temporal space. If smooth temporal behavior of the strains can be assumed, then the disturbance level can be efficiently reduced by filtering it in the time domain (Figure 7.8).

The highest von Mises strains were found at the superior head-neck junction where the strains were mostly tensile. For the majority of the bones, the highest strains were around 2 % at the moment of the fracture. One bone was an exception since its maximum strain at the time of fracture was almost two times higher and its yield-to-fracture phase was longer than that encountered in the other bones. However, since this bone was not an outlier in terms of any other parameters, its strain bearing ability and ductility were properties of its material. In addition, one bone was stiffer than the other bones. Taken together, this highlights that caution is needed when using composite bones for validation purposes.

Under the same load, the inter-sample variation (SD/mean) of the surface strains was 20-25 %. The inter-sample variation was much higher for strain values below 0.3 %, probably due to the smaller signal-to-noise ratio. When the strain values were normalized by the maximum strain value, the inter-sample variation was 5-10 %.

The maximum load of the femur during normal stance is obtained in about 0.33s [196] which leads to a physiological loading

rate of $\sim$2.0 mm/s [64]. The frame rate of the DIC device (4 Hz) limited the usable loading rates. However, the strains on the femur are highly linear at physiological loading rates [64]. Some non-linearity takes place at moderate loading rates of 0.5 mm/s [206], but the non-linearity is still relatively low at very low loading rates (0.5 mm/min) [26]. In addition, it has been proposed that this non-linearity is mostly due to micro-fractures preceding the macro scale fracture, and thus not to non-linearity in the actual material [64]. High-speed cameras enable the use of physiological loading rates with DIC, and make it possible to capture the strains occuring during fracture.

The DIC technique provides superior datasets for validation of finite element models (10000-50000 data points) [162]. However, it must be noted that DIC measures only surface strains, whereas the strains calculated by finite element models are three-dimensional [154].

9 Summary and conclusions

In this thesis, a method to reconstruct the 3D surface and internal density distribution of a proximal femur based on one 2D image, and a method to estimate the 3D orientation of a femur in a 2D image were developed and evaluated. In addition, the surface strains of composite femurs were measured during a mechanical compression test. The validity of the developed methods and their outputs were critically discussed.

The main conclusions from this thesis may be summarized as follows:

- The 3D shape and the internal density distribution of a proximal femur can be accurately reconstructed by using *a priori* information and one DXA image.
- The reconstructed 3D shape provides a valid input for patient-specific mechanical simulation intended to predict the strength of the femur.
- 2D SAM and ANN-based predictive model can estimate the 3D rotation of a femur in 2D radiographs with three times higher accuracy compared with visual analysis of trained expert. Therefore, the method has a good potential to differentiate the amount of femur rotations between two different image sets.
- Measurement of the surface strains on the whole surface of the femur during mechanical testing provides accurate information about the mechanical characteristics of femur. The measured strains can reveal, differentiate, and explain sample-to-sample differences.
- All these methods have potential to contribute to the diagnosis of osteoporosis in the future.

Bibliography

[1] J. A. Buckwalter, M. J. Glimcher, R. R. Cooper, and R. Recker, "Bone biology. I: Structure, blood supply, cells, matrix, and mineralization," *The Journal of Bone and Joint Surgery* **77,** 1256–1275 (1995).

[2] J. A. Buckwalter, M. Glimcher, R. Cooper, and R. Recker, "Bone biology. II: Formation, form, modeling, remodeling, and regulation of cell function," *Journal of bone and joint surgery* **77,** 1276–1289 (1995).

[3] J. Wolff, "Ueber die innere Architectur der Knochen und ihre Bedeutung für die Frage vom Knochenwachsthum," *Archiv für pathologische Anatomie und Physiologie und für klinische Medicin* **50,** 389–450 (1870).

[4] J. Wolff, "The classic: on the inner architecture of bones and its importance for bone growth. 1870.," *Clinical orthopaedics and related research* **468,** 1056–1065 (2010).

[5] WHO, "Assessment of fracture risk and its application to screening for postmenopausal osteoporosis. Report of a WHO Study Group," *WHO Technical Report Series* **843,** 1–129 (1994).

[6] Consensus Development Conference:, "Prophylaxis and treatment of osteoporosis," *Osteoporosis international* **1,** 114–117 (1991).

[7] J. A. Kanis, E. V. McCloskey, H. Johansson, A. Oden, L. J. Melton, and N. Khaltaev, "A reference standard for the description of osteoporosis.," *Bone* **42,** 467–475 (2008).

[8] T. D. Rachner, S. Khosla, and L. C. Hofbauer, "Osteoporosis: now and the future.," *Lancet* **377,** 1276–1287 (2011).

[9] C. Cooper, "Epidemiology of osteoporosis," *Osteoporosis international* **2,** S2–S8 (1999).

[10] J.-Y. Reginster and N. Burlet, "Osteoporosis: a still increasing prevalence.," *Bone* **38,** S4–S9 (2006).

[11] L. J. Melton, E. A. Chrischilles, C. Cooper, A. W. Lane, and B. L. Riggs, "How Many Women Have Osteoporosis?," *Journal of Bone and Mineral Research* **7,** 1005–1010 (1992).

[12] O. Johnell and J. A. Kanis, "An estimate of the worldwide prevalence and disability associated with osteoporotic fractures.," *Osteoporosis international* **17,** 1726–1733 (2006).

[13] J. A. Kanis and O. Johnell, "Requirements for DXA for the management of osteoporosis in Europe.," *Osteoporosis international* **16,** 229–238 (2005).

[14] R. Burge, B. Dawson-Hughes, D. Solomon, J. Wong, A. King, and A. Tosteson, "Incidence and economic burden of osteoporosis-related fractures in the United States, 2005-2025," *Journal of Bone and Mineral Research* **22,** 465–475 (2007).

[15] J. A. Cauley, "Public health impact of osteoporosis," *The journals of gerontology. Series A, Biological sciences and medical sciences* **68,** 1243–1251 (2013).

[16] J. A. Kanis, N. Burlet, C. Cooper, P. D. Delmas, J.-Y. Reginster, F. Borgstrom, and R. Rizzoli, "European guidance for the diagnosis and management of osteoporosis in postmenopausal women.," *Osteoporosis international* **19,** 399–428 (2008).

[17] A. Cranney, S. A. Jamal, J. F. Tsang, R. G. Josse, and W. D. Leslie, "Low bone mineral density and fracture burden in postmenopausal women," *Canadian Medical Association journal* **177,** 575–580 (2007).

[18] K. L. Stone, D. G. Seeley, L.-Y. Lui, J. A. Cauley, K. Ensrud, W. S. Browner, M. C. Nevitt, and S. R. Cummings, "BMD at multiple sites and risk of fracture of multiple types : long-term results from the study of osteoporotic fractures," *Journal of Bone and Mineral Research* **18,** 1947–1954 (2003).

[19] J. A. Pasco, E. Seeman, M. J. Henry, E. N. Merriman, G. C. Nicholson, and M. A. Kotowicz, "The population burden of fractures originates in women with osteopenia, not osteoporosis," *Osteoporosis international* **17,** 1404–1409 (2006).

[20] E. Seeman and P. D. Delmas, "Bone quality–the material and structural basis of bone strength and fragility," *The New England journal of medicine* **354,** 2250–2261 (2006).

[21] E. Seeman, "Bone quality: the material and structural basis of bone strength," *Journal of bone and mineral metabolism* **26,** 1–8 (2008).

[22] J. Compston, "Bone quality: what is it and how is it measured?," *Arquivos brasileiros de endocrinologia e metabologia* **50,** 579–585 (2006).

[23] E. S. Orwoll, L. M. Marshall, C. M. Nielson, S. R. Cummings, J. Lapidus, J. A. Cauley, K. Ensrud, N. Lane, P. R. Hoffmann, D. L. Kopperdahl, and T. M. Keaveny, "Finite element analysis of the proximal femur and hip fracture risk in older men," *Journal of Bone and Mineral Research* **24,** 475–483 (2009).

[24] E. Schileo, F. Taddei, A. Malandrino, L. Cristofolini, and M. Viceconti, "Subject-specific finite element models can accurately predict strain levels in long bones," *Journal of biomechanics* **40,** 2982–2989 (2007).

[25] L. Grassi, E. Schileo, F. Taddei, L. Zani, M. Juszczyk, L. Cristofolini, and M. Viceconti, "Accuracy of finite element predictions in sideways load configurations for the proximal human femur.," *Journal of biomechanics* **45,** 394–399 (2012).

[26] M. Bessho, I. Ohnishi, J. Matsuyama, T. Matsumoto, K. Imai, and K. Nakamura, "Prediction of strength and strain of the proximal femur by a CT-based finite element method," *Journal of biomechanics* **40,** 1745–1753 (2007).

[27] Z. Yosibash, R. Padan, L. Joskowicz, and C. Milgrom, "A CT-based high-order finite element analysis of the human proximal femur compared to in-vitro experiments," *Journal of biomechanical engineering* **129,** 297–309 (2007).

[28] J. H. Keyak, "Comparison of in situ and in vitro CT scan-based finite element model predictions of proximal femoral fracture load," *Medical Engineering and Physics* **25,** 781–787 (2003).

[29] D. D. Cody, G. J. Gross, F. J. Hou, H. J. Spencer, S. A. Goldstein, and D. P. Fyhrie, "Femoral strength is better predicted by finite element models than QCT and DXA," *Journal of Biomechanics* **32,** 1013–1020 (1999).

[30] T. Keaveny, D. Kopperdahl, L. Melton III, P. Hoffmann, S. Amin, B. Riggs, and S. Khosla, "Age-dependence of femoral strength in white women and men," *Journal of Bone and Mineral Research* **25,** 994–1001 (2010).

[31] D. C. Wirtz, T. Pandorf, F. Portheine, K. Radermacher, N. Schiffers, A. Prescher, D. Weichert, and F. U. Niethard, "Concept and development of an orthotropic FE model of the proximal femur," *Journal of biomechanics* **36,** 289–293 (2003).

[32] E. Schileo, F. Taddei, L. Cristofolini, and M. Viceconti, "Subject-specific finite element models implementing a maximum principal strain criterion are able to estimate failure risk and fracture location on human femurs tested in vitro," *Journal of biomechanics* **41,** 3563–67 (2008).

[33] E. Schileo, E. Dall'ara, F. Taddei, A. Malandrino, T. Schotkamp, M. Baleani, and M. Viceconti, "An accurate estimation of bone density improves the accuracy of subject-specific finite element models," *Journal of biomechanics* **41,** 2483–2491 (2008).

[34] J. Damilakis, J. E. Adams, G. Guglielmi, and T. M. Link, "Radiation exposure in X-ray-based imaging techniques used in osteoporosis," *European radiology* **20,** 2707–2714 (2010).

[35] S. Kolta, A. Le Bras, D. Mitton, V. Bousson, J. a. de Guise, J. Fechtenbaum, J. D. Laredo, C. Roux, and W. Skalli, "Three-dimensional X-ray absorptiometry (3D-XA): a method for reconstruction of human bones using a dual X-ray absorptiometry device," *Osteoporosis international* **16,** 969–976 (2005).

[36] C. M. Langton, S. Pisharody, and J. H. Keyak, "Generation of a 3D proximal femur shape from a single projection 2D radiographic image," *Osteoporosis international* **20,** 455–61 (2009).

[37] G. Zheng, M. A. G. Ballester, M. Styner, and L.-P. Nolte, "Reconstruction of patient-specific 3D bone surface from 2D calibrated fluoroscopic images and point distribution model," in *Medical Image Computing and Computer-Assisted Intervention-MICCAI 2006* (2006), pp. 25–32.

[38] P. E. Galibarov, P. J. Prendergast, and a. B. Lennon, "A method to reconstruct patient-specific proximal femur surface models from planar pre-operative radiographs," *Medical engineering and physics* **32,** 1180–1188 (2010).

[39] L. Humbert, T. Whitmarsh, M. De Craene, L. M. del Rio Barquero, K. D. Fritscher, R. Schubert, F. Eckstein, T. Link, and A. F. Frangi, "3D reconstruction of both shape and Bone Mineral Density distribution of the femur from DXA images," in *2010 IEEE International Symposium on Biomedical Imaging: From Nano to Macro* (2010), pp. 456–459.

[40] J. Thevenot, J. Koivumäki, V. Kuhn, F. Eckstein, and T. Jämsä, "A novel methodology for generating 3D finite element models of the hip from 2D radiographs," *Journal of Biomechanics* **47,** 438–444 (2013).

[41] Correlated Solutions, "Vic-3D 2010 testing guide,", Technical report, Correlated Solutions.

[42] R. Alexander, R. Ker, and M. Bennett, "Optimum stiffness for leg bones," *Journal of Zoology* **222,** 471–478 (1990).

[43] H. Isaksson, W. Wilson, C. C. Van Donkelaar, R. Huiskes, and K. Ito, "Comparison of biophysical stimuli for mechano-regulation of tissue differentiation during fracture healing," *Journal of Biomechanics* **39,** 1507–1516 (2006).

[44] OpenStax College, "Anatomy and Physiology," Retrieved Mars 6, 2014, from http://cnx.org/content/col11496/1.6/ (2013).

[45] Creative Commons, "Creative Commons Attribution 3.0 Unported lisence," Retrieved Mars 6, 2014, from http://creativecommons.org/licenses/by/3.0/deed.en (2014).

[46] S. L. Teitelbaum, "The osteoclast and its unique cytoskeleton," *Annals of the New York Academy of Sciences* **1240,** 14–17 (2011).

[47] R. Marcus, D. Feldman, D. Nelson, and C. Rosen, eds., *Fundamentals of osteoporosis* (Academic Press, 2010).

[48] P. Downey and M. Siegel, "Bone biology and the clinical implications for osteoporosis," *Physical therapy* **86,** 77–91 (2006).

[49] S. Khosla, "Minireview: The opg/rankl/rank system," *Endocrinology* **142,** 5050–5055 (2001).

[50] J. Aubin and E. Bonnelye, "Osteoprotegerin and its ligand: a new paradigm for regulation of osteoclastogenesis and bone resorption," *Osteoporosis international* **11,** 905–913 (2000).

[51] R. Huiskes, R. Ruimerman, G. H. van Lenthe, and J. D. Janssen, "Effects of mechanical forces on maintenance and adaptation of form in trabecular bone.," *Nature* **405,** 704–6 (2000).

[52] S. Tassani, C. Ohman, F. Baruffaldi, M. Baleani, and M. Viceconti, "Volume to density relation in adult human bone tissue.," *Journal of biomechanics* **44,** 103–8 (2011).

[53] A. Hoshino and W. Wallace, "Impact-absorbing properties of the human knee," *Journal of Bone and Joint Surgery* **69,** 807–811 (1987).

[54] M. Kerschnitzki, P. Kollmannsberger, M. Burghammer, G. N. Duda, R. Weinkamer, W. Wagermaier, and P. Fratzl, "Architecture of the osteocyte network correlates with bone material quality.," *Journal of bone and mineral research* **28,** 1837–1845 (2013).

[55] J. a. Gargac, T. L. Turnbull, R. K. Roeder, and G. L. Niebur, "A probabilistic damage model based on direct 3-D correlation of strain to damage formation following fatigue loading of rat femora.," *Journal of the mechanical behavior of biomedical materials* **30,** 234–243 (2013).

[56] J. D. Currey, "Bone architecture and fracture.," *Current osteoporosis reports* **3,** 52–56 (2005).

[57] J. D. Currey, "Measurement of the mechanical properties of bone: a recent history," *Clinical orthopaedics and related research* **467,** 1948–1954 (2009).

[58] W. Hayes, "Biomechanics of cortical and trabecular bone: implications for assessment of fracture risk," in *Basic orthopaedic biomechanics* (Raven, New York, 1991), pp. 93–142.

[59] D. T. Reilly and A. H. Burstein, "The Mechanical Properties of Cortical Bone," *The Journal of Bone and Joint Surgery* **56,** 1001–1022 (1974).

[60] T. M. Wright and W. C. Hayes, "Tensile testing of bone over a wide range of strain rates: effects of strain rate, microstructure and density," *Medical and biological engineering* **14,** 671–680 (1976).

[61] R. S. Lakes, J. L. Katz, and S. S. Sternstein, "Viscoelastic properties of wet cortical bone-I. Torsional and biaxial studies," *Journal of Biomechanics* **12,** 657–678 (1979).

[62] R. S. Lakes and J. L. Katz, "Viscoelastic properties of wet cortical bone-II. Relaxation mechanisms," *Journal of Biomechanics* **12,** 679–687 (1979).

[63] B. Helgason, E. Perilli, E. Schileo, F. Taddei, S. Brynjólfsson, and M. Viceconti, "Mathematical relationships between bone density and mechanical properties: a literature review," *Clinical biomechanics* **23,** 135–146 (2008).

[64] M. Juszczyk, L. Cristofolini, and M. Viceconti, "The human proximal femur behaves linearly elastic up to failure under physiological loading conditions," *Journal of biomechanics* **44,** 2259–2266 (2011).

[65] D. T. Reilly and a. H. Burstein, "The elastic and ultimate properties of compact bone tissue," *Journal of biomechanics* **8,** 393–405 (1975).

[66] I. Oh and W. H. Harris, "Proximal strain distribution in the loaded femur. An in vitro comparison of the distributions in the intact femur and after insertion of different hip-replacement femoral components," *The Journal of bone and joint surgery. American volume* **60,** 75–85 (1978).

[67] R. Huiskes, J. Janssen, and T. Slooff, "A detailed comparison of experimental and theoretical stress-analyses of a human femur," *Mechanical properties of Bone* **45,** 211–234 (1981).

[68] C. Kukla, C. Gaebler, R. Pichl, R. Prokesch, G. Heinze, and T. Heinz, "Predictive geometric factors in a standardized model of femoral neck fracture," *Injury* **33,** 427–433 (2002).

[69] G. Holzer, G. Von Skrbensky, L. Holzer, and W. Pichl, "Hip fractures and the contribution of cortical versus trabecular bone to femoral neck strength," *Journal of bone and mineral research* **24,** 468–474 (2009).

[70] L. Cristofolini, M. Juszczyk, F. Taddei, and M. Viceconti, "Strain distribution in the proximal human femoral metaphysis," *Proceedings of the Institution of Mechanical Engineers, Part H: Journal of Engineering in Medicine* **223,** 273–288 (2009).

[71] A. Courtney, E. Wachtel, E. Myers, and W. Hayes, "Effects of loading rate on strength of the proximal femur," *Calcified tissue international* **55,** 53–58 (1994).

[72] A. C. Courtney, E. F. Wachtel, E. R. Myers, and W. C. Hayes, "Age-related reductions in the strength of the femur tested in a fall-loading configuration," *The Journal of bone and joint surgery. American volume* **77,** 387–95 (1995).

[73] P. M. de Bakker, S. L. Manske, V. Ebacher, T. R. Oxland, P. A. Cripton, and P. Guy, "During sideways falls proximal femur fractures initiate in the superolateral cortex: evidence from high-speed video of simulated fractures," *Journal of biomechanics* **42,** 1917–25 (2009).

[74] J. E. M. Koivumäki, J. Thevenot, P. Pulkkinen, V. Kuhn, T. M. Link, F. Eckstein, and T. Jämsä, "Cortical Bone Finite Element Models in the Estimation of Experimentally Measured Failure Loads in the Proximal Femur," *Bone* **51,** 737–740 (2012).

[75] F. Eckstein, E. Lochmüller, C. Lill, V. Kuhn, E. Schneider, G. Delling, and R. Müller, "Bone strength at clinically relevant sites displays substantial heterogeneity and is best predicted from site-specific bone densitometry," *Journal of Bone and Mineral Research* **17,** 162–171 (2002).

[76] T. M. Link, V. Vieth, R. Langenberg, N. Meier, A. Lotter, D. Newitt, and S. Majumdar, "Structure analysis of high resolution magnetic resonance imaging of the proximal femur: in vitro correlation with biomechanical strength and BMD," *Calcified tissue international* **72,** 156–65 (2003).

[77] Consensus Development Conference:, "Diagnosis, Prophylaxis, and Treatment of Osteoporosis," *American Journal of Medicine* **94,** 646–650 (1993).

[78] H. G. Ahlborg, O. Johnell, C. H. Turner, G. Rannevik, and M. K. Karlsson, "Bone loss and bone size after menopause," *The New England journal of medicine* **349,** 327–34 (2003).

[79] E. Donnelly, "Methods for Assessing Bone Quality: A Review," *Clinical orthopaedics and related research* **469,** 2128–2138 (2010).

[80] J. A. Kanis, A. Oden, O. Johnell, C. De Laet, B. Jonsson, and A. Oglesby, "The components of excess mortality after hip fracture," *Bone* **32,** 468–473 (2003).

[81] P. N. Sambrook and C. Cooper, "Osteoporosis.," *Lancet* **367,** 2010–2018 (2006).

[82] T. Meling, K. Harboe, and K. Sø reide, "Incidence of traumatic long-bone fractures requiring in-hospital management: a prospective age- and gender-specific analysis of 4890 fractures," *Injury* **40,** 1212–1219 (2009).

[83] Office of the Surgeon General (US), *Bone Health and Osteoporosis: A Report of the Surgeon General* (Office of the Surgeon General (US), 2004).

[84] W. D. Leslie and L. M. Lix, "Comparison between various fracture risk assessment tools," *Osteoporosis international* **25,** 1–21 (2014).

[85] S. L. Bonnick, "HSA: beyond BMD with DXA.," *Bone* **41,** S9–S12 (2007).

[86] J. A. Kanis, "Diagnosis of osteoporosis and assessment of fracture risk," *Lancet* **359,** 1929–1936 (2002).

[87] J. A. Kanis, O. Johnell, A. Oden, B. Jonsson, C. De Laet, and A. Dawson, "Risk of hip fracture according to the World Health Organization criteria for osteopenia and osteoporosis," *Bone* **27,** 585–590 (2000).

[88] P. M. Cawthon, S. K. Ewing, D. C. Mackey, H. A. Fink, S. R. Cummings, K. E. Ensrud, M. L. Stefanick, D. C. Bauer, J. A. Cauley, and E. S. Orwoll, "Change in hip bone mineral density and risk of subsequent fractures in older men," *Journal of bone and mineral research* **27,** 2179–2188 (2012).

[89] D. Marshall, O. Johnell, and H. Wedel, "Meta-analysis of how well measures of bone mineral density predict occurrence of osteoporotic fractures," *BMJ* **312,** 1254–1259 (1996).

[90] P. Pulkkinen, J. Partanen, P. Jalovaara, and T. Jämsä, "BMD T-score discriminates trochanteric fractures from unfractured controls, whereas geometry discriminates cervical fracture cases from unfractured controls of similar BMD," *Osteoporosis international* **21,** 1269–1276 (2010).

[91] E. Lochmüller, J. Zeller, D. Kaiser, F. Eckstein, J. Landgraf, R. Putz, and R. Steldinger, "Correlation of femoral and lumbar DXA and calcaneal ultrasound, measured in situ with intact soft tissues, with the in vitro failure loads of the proximal femur," *Osteoporosis international* **8,** 591–598 (1998).

[92] A. Unnanuntana, B. P. Gladnick, E. Donnelly, and J. M. Lane, "The assessment of fracture risk," *The Journal of bone and joint surgery. American volume* **92,** 743–753 (2010).

[93] S. C. E. Schuit, M. van der Klift, A. E. A. M. Weel, C. E. D. H. de Laet, H. Burger, E. Seeman, A. Hofman, A. G. Uitterlinden, J. P. T. M. van Leeuwen, and H. A. P. Pols, "Fracture incidence and association with bone mineral density in elderly men and women: the Rotterdam Study," *Bone* **34,** 195–202 (2004).

[94] J. a. Kanis, A. Oden, H. Johansson, F. Borgström, O. Ström, and E. McCloskey, "FRAX and its applications to clinical practice.," *Bone* **44,** 734–43 (2009).

[95] J. Sirola, T. Rikkonen, M. Tuppurainen, J. S. Jurvelin, and H. Kröger, "Association of grip strength change with menopausal bone loss and related fractures: a population-based follow-up study," *Calcified tissue international* **78,** 218–226 (2006).

[96] T. Rikkonen, J. Sirola, K. Salovaara, M. Tuppurainen, J. S. Jurvelin, R. Honkanen, and H. Kröger, "Muscle strength and body composition are clinical indicators of osteoporosis," *Calcified tissue international* **91,** 131–138 (2012).

[97] J. A. Kanis, O. Johnell, A. Oden, H. Johansson, and E. McCloskey, "FRAX and the assessment of fracture probability in men and women from the UK," *Osteoporosis international* **19,** 385–397 (2008).

[98] J. A. Kanis, A. Oden, O. Johnell, H. Johansson, C. De Laet, J. Brown, P. Burckhardt, C. Cooper, C. Christiansen, S. Cummings, J. A. Eisman, S. Fujiwara, C. Glüer, D. Goltzman, D. Hans, M.-A. Krieg, A. La Croix, E. McCloskey, D. Mellstrom, L. J. Melton, H. Pols, J. Reeve, K. Sanders, A.-M. Schott, A. Silman, D. Torgerson, T. van Staa, N. B. Watts, and N. Yoshimura, "The use of clinical risk factors enhances the performance of BMD in the prediction of hip and osteoporotic fractures in men and women.," *Osteoporosis international* **18,** 1033–1046 (2007).

[99] J. S. Gregory and R. M. Aspden, "Femoral geometry as a risk factor for osteoporotic hip fracture in men and women," *Medical engineering and physics* **30,** 1275–1286 (2008).

[100] J. Partanen, T. Jämsä, and P. Jalovaara, "Influence of the upper femur and pelvic geometry on the risk and type of hip fractures.," *Journal of bone and mineral research* **16,** 1540–1546 (2001).

[101] F. Rivadeneira, M. C. Zillikens, C. E. D. Laet, A. Hofman, A. G. Uitterlinden, T. J. Beck, and H. A. Pols, "Femoral neck BMD is a strong predictor of hip fracture susceptibility in elderly men and women because it detects cortical bone instability: the Rotterdam study," *Journal of Bone and Mineral Research* **22,** 1781–1790 (2007).

[102] J. Y. Anderson and E. Trinkaus, "Patterns of sexual, bilateral and interpopulational variation in human femoral neck-shaft angles," *Journal of anatomy* **192,** 279–85 (1998).

[103] T. Link, S. Majumdar, S. Grampp, G. Guglielmi, C. van Kuijk, H. Imhof, C. Glueer, and J. E. Adams, "Imaging of trabecular bone structure in osteoporosis," *European radiology* **9,** 1781–1788 (1999).

[104] T. Vokes, D. Lauderdale, S.-L. Ma, M. Chinander, K. Childs, and M. Giger, "Radiographic texture analysis of densitometric calcaneal images: relationship to clinical characteristics and to bone fragility," *Journal of bone and mineral research* **25,** 56–63 (2010).

[105] J. Thevenot, J. Hirvasniemi, M. Finnilä, P. Pulkkinen, V. Kuhn, T. Link, F. Eckstein, T. Jämsä, and S. Saarakkala, "Trabecular homogeneity index derived from plain radiograph to evaluate bone quality," *Journal of bone and mineral research* **28,** 2584–2591 (2013).

[106] B. C. Silva, W. D. Leslie, H. Resch, O. Lamy, O. Lesnyak, N. Binkley, E. V. McCloskey, J. a. Kanis, and J. P. Bilezikian, "Trabecular Bone Score: A Non-Invasive Analytical Method Based Upon the DXA Image," *Journal of bone and mineral research* **29,** 518–530 (2014).

[107] J. Compston, A. Cooper, C. Cooper, R. Francis, J. A. Kanis, D. Marsh, E. V. McCloskey, D. M. Reid, P. Selby, and M. Wilkins, "Guidelines for the diagnosis and management of osteoporosis in postmenopausal women and men from the age of 50 years in the UK," *Maturitas* **62,** 105–108 (2009).

[108] W. Röntgen, "On a new kind of rays," *Science* **3,** 227–231 (1896).

[109] W. Röntgen, "Über eine neue Art von Strahlen," *Annalen der Physik* (1896).

[110] H. Hull, Q. He, J. Thornton, F. Javed, L. Allen, J. Wang, R. N. Pierson, and D. Gallagher, "iDXA, Prodigy, and DPXL dual-energy X-ray absorptiometry whole-body scans: a cross-calibration study," *Journal of clinical densitometry* **12,** 95–102 (2009).

[111] G. Hounsfield, "Computerized transverse axial scanning (tomography): Part I. Description of system," *The British journal of radiology* **46,** 1016–1022 (1973).

[112] J. E. Adams, "Quantitative computed tomography," *Eur J Radiol* **71,** 415–424 (2009).

[113] H. H. Bayraktar, E. F. Morgan, G. L. Niebur, G. E. Morris, E. K. Wong, and T. M. Keaveny, "Comparison of the elastic and yield properties of human femoral trabecular and cortical bone tissue," *Journal of biomechanics* **37,** 27–35 (2004).

[114] B. Helgason, F. Taddei, H. Pálsson, E. Schileo, L. Cristofolini, M. Viceconti, and S. Brynjólfsson, "A modified method for assigning material properties to FE models of bones," *Medical engineering and physics* **30,** 444–453 (2008).

[115] E. F. Morgan, "Trabecular bone modulusden-density relationships depend on anatomic site," *Journal of Biomechanics* **36,** 897–904 (2003).

[116] F. Taddei, A. Pancanti, and M. Viceconti, "An improved method for the automatic mapping of computed tomography numbers onto finite element models," *Medical Engineering and Physics* **26,** 61–69 (2004).

[117] F. Taddei, E. Schileo, B. Helgason, L. Cristofolini, and M. Viceconti, "The material mapping strategy influences the accuracy of CT-based finite element models of bones: an evaluation against experimental measurements," *Medical engineering and physics* **29,** 973–979 (2007).

[118] C. Zannoni, R. Mantovani, and M. Viceconti, "Material properties assignment to finite element models of bone structures: a new method," *Medical engineering and physics* **20,** 735–740 (1998).

[119] T. F. Lang, J. H. Keyak, M. W. Heitz, P. Augat, Y. Lu, A. Mathur, and H. K. Genant, "Volumetric quantitative computed tomography of the proximal femur: precision and relation to bone strength," *Bone* **21,** 101–108 (1997).

[120] X. G. Cheng, G. Lowet, S. Boonen, P. H. Nicholson, P. Brys, J. Nijs, and J. Dequeker, "Assessment of the strength of proximal femur in vitro: relationship to femoral bone mineral density and femoral geometry," *Bone* **20,** 213–218 (1997).

[121] V. Bousson, A. Le Bras, F. Roqueplan, Y. Kang, D. Mitton, S. Kolta, C. Bergot, W. Skalli, E. Vicaut, W. Kalender, K. Engelke, and J.-D. Laredo, "Volumetric quantitative computed tomography of the proximal femur: relationships linking geometric and densitometric variables to bone strength. Role for compact bone," *Osteoporosis international* **17,** 855–864 (2006).

[122] National Electrical Manufacturers Association, "PS 3.3-2011 Digital Imaging and Communications in Medicine (DICOM) Part 3: Information Object Definitions," (2011).

[123] P. Pisani, M. D. Renna, F. Conversano, E. Casciaro, M. Muratore, E. Quarta, M. D. Paola, and S. Casciaro, "Screening and early diagnosis of osteoporosis through X-ray and ultrasound based techniques," *World journal of radiology* **5,** 398–410 (2013).

[124] C. M. Langton, S. Palmer, and R. Porter, "The measurement of broadband ultrasonic attenuation in cancellous bone," *Engineering in medicine* **13,** 89–91 (1984).

[125] D. Hans, P. Dargent-Molina, a. M. Schott, J. L. Sebert, C. Cormier, P. O. Kotzki, P. D. Delmas, J. M. Pouilles, G. Breart, and P. J. Meunier, "Ultrasonographic heel measurements to predict hip fracture in elderly women: the EPIDOS prospective study," *Lancet* **348,** 511–514 (1996).

[126] M. K. H. Malo, J. P. Karjalainen, H. Isaksson, O. Riekkinen, J. S. Jurvelin, and J. Töyräs, "Numerical analysis of uncertainties in dual frequency bone ultrasound technique," *Ultrasound in medicine and biology* **36,** 288–294 (2010).

[127] J. P. Karjalainen, O. Riekkinen, J. Töyräs, M. Hakulinen, H. Kröger, T. Rikkonen, K. Salovaara, and J. S. Jurvelin, "Multi-site bone ultrasound measurements in elderly women with and without previous hip fractures," *Osteoporosis international* **23,** 1287–1295 (2012).

[128] I. L. Dryden and K. V. Mardia, *Statistical Analysis of Shape* (Wiley, 1998).

[129] J. Gower, "Generalized procrustes analysis," *Psychometrika* **40,** 33–51 (1975).

[130] F. Bookstein, "Principal warps: Thin-plate splines and the decomposition of deformations," *Pattern Analysis and Machine Intelligence, IEEE Transactions on* **11,** 567–585 (1989).

[131] R. Brooks and T. Arbel, "Improvements to the itk:: KernelTransform and subclasses," *Insight Journal* 1–6 (2007).

[132] K. Pearson, "On lines and planes of closest fit to systems of points in space," *Philosophical Magazine* **2,** 559–572 (1901).

[133] H. Hotelling, "Analysis of a complex of statistical variables into principal components," *Journal of Educational Psychology* **24,** 417–441 (1933).

[134] C. Eckart and G. Young, "The approximation of one matrix by another of lower rank," *Psychometrika* **1,** 211–218 (1936).

[135] T. Cootes, C. Taylor, D. Cooper, and J. Graham, "Active shape models-their training and application," *Computer vision and image understanding* **61,** 38–59 (1995).

[136] N. Sarkalkan, H. Weinans, and A. A. Zadpoor, "Statistical shape and appearance models of bones," *Bone* **60,** 129–140 (2014).

[137] T. Cootes and C. Taylor, "Statistical models of appearance for medical image analysis and computer vision," in *Proc. SPIE Medical Imaging*, Vol. 4322 (2001), pp. 236–248.

[138] T. Cootes, G. Edwards, and C. Taylor, "Active appearance models," *IEEE Transactions on Pattern Analysis and Machine Intelligence* **23,** 681–685 (2001).

[139] W. McCulloch and W. Pitts, "A logical calculus of the ideas immanent in nervous activity," *The bulletin of mathematical biophysics* **5,** 115–133 (1943).

[140] B. Bose, "Neural network applications in power electronics and motor drives-An introduction and perspective," *IEEE Transactions on Industrial Electronics* **54,** 14–33 (2007).

[141] B. M. Wilamowski, "Neural Networks and Fuzzy Systems for Nonlinear Applications," in *Intelligent Engineering Systems, 2007, 11th International conference on intelligent engineering systems* (2007), pp. 13–19.

[142] B. M. Wilamowski, "Neural network architectures and learning algorithms," *Industrial Electronics Magazine* **3,** 56–63 (2009).

[143] B. M. Wilamowski, D. Hunter, and A. Malinowski, "Solving parity-N problems with feedforward neural networks," in *Neural Networks, 2003. Proceedings of the International Joint Conference on. IEEE, 2003.* (2003), pp. 2546–2551.

[144] C. Darwin, *The origin of species* (John Murray, 1859).

[145] P. Larranaga, C. Kuijpers, R. Murga, and I. Inza, "Genetic algorithms for the travelling salesman problem: A review of representations and operators," *Artificial Intelligence Review* **13,** 129–170 (1999).

[146] D. Whitley, "A genetic algorithm tutorial," *Statistics and Computing* **4,** 65–85 (1994).

[147] M. A. Sutton, J.-J. Orteu, and H. Schreier, *Image Correlation for Shape, Motion and Deformation Measurements: Basic Concepts, Theory and Applications* (Springer, Boston, MA, 2009).

[148] W. D. Lockwood, B. Tomaz, and A. P. Reynolds, "Mechanical response of friction stir welded AA2024: experiment and modeling," *Materials Science and Engineering* **323,** 348–353 (2002).

[149] A. A. Zadpoor, J. Sinke, and R. Benedictus, "Finite element modeling and failure prediction of friction stir welded blanks," *Materials and Design* **30,** 1423–1434 (2009).

[150] L. Cristofolini, G. Conti, M. Juszczyk, S. Cremonini, S. Van Sint Jan, and M. Viceconti, "Structural behaviour and strain distribution of the long bones of the human lower limbs," *Journal of biomechanics* **43,** 826–835 (2010).

[151] N. Trabelsi, Z. Yosibash, C. Wutte, P. Augat, and S. Eberle, "Patient-specific finite element analysis of the human femur-A double-blinded biomechanical validation," *Journal of biomechanics* **44,** 1666–1672 (2011).

[152] J. Op Den Buijs and D. Dragomir-Daescu, "Validated finite element models of the proximal femur using two-dimensional projected geometry and bone density," *Computer methods and programs in biomedicine* **104,** 168–174 (2011).

[153] S. Amin Yavari, J. van der Stok, H. Weinans, and A. A. Zadpoor, "Full-field strain measurement and fracture analysis of rat femora in compression test," *Journal of biomechanics* **46,** 1282–1292 (2013).

[154] A. S. Dickinson, A. C. Taylor, H. Ozturk, and M. Browne, "Experimental validation of a finite element model of the proximal femur using digital image correlation and a composite bone model," *Journal of biomechanical engineering* **133,** 014504 (2011).

[155] S. Gilchrist, P. Guy, and P. a. Cripton, "Development of an inertia-driven model of sideways fall for detailed study of femur fracture mechanics," *Journal of biomechanical engineering* **135,** 121001 (2013).

[156] W. Brekelmans, H. Poort, and T. Slooff, "A new method to analyse the mechanical behaviour of skeletal parts," *Acta Orthopaedica Scandinavica* **43,** 301–317 (1972).

[157] A. Liu and B. Joe, "Relationship between tetrahedron shape measures," *BIT Numerical Mathematics* **34,** 268–287 (1994).

[158] M. Bern, D. Eppstein, and J. Gilbert, "Provably good mesh generation," *Journal of Computer and System Sciences* **48,** 384–409 (1994).

[159] ANSYS, "Mechanical APDL Theory Reference Release 14.5,", Technical Report October, ANSYS, Inc, Southpointe 275 Technology Drive Canonsburg, PA 15317.

[160] S. Eberle, M. Göttlinger, and P. Augat, "An investigation to determine if a single validated density-elasticity relationship can be used for subject specific finite element analyses of human long bones," *Medical engineering and physics* **35,** 875–883 (2013).

[161] L. Cristofolini, E. Schileo, M. Juszczyk, F. Taddei, S. Martelli, and M. Viceconti, "Mechanical testing of bones: the positive synergy of finite-element models and in vitro experiments," *Philosophical transactions. Series A, Mathematical, physical, and engineering sciences* **368,** 2725–2763 (2010).

[162] L. Grassi, S. P. Väänänen, S. Amin Yavari, H. Weinans, J. S. Jurvelin, A. A. Zadpoor, and H. Isaksson, "Experimental validation of finite element model for proximal composite femur using optical measurements," *Journal of the mechanical behavior of biomedical materials* **21,** 86–94 (2013).

[163] R. J. Allemang and D. Brown, "A correlation coefficient for modal vector analysis," in *Proceedings, International Modal Analysis Conference* (1982), pp. 110–116.

[164] R. J. Allemang, "The modal assurance criterion-twenty years of use and abuse," *Sound and Vibration* **37,** 14–23 (2003).

[165] M. Pastor, M. Binda, and T. Harčarik, "Modal Assurance Criterion," *Procedia Engineering* **48,** 543–548 (2012).

[166] P. Markelj, D. Tomaževič, B. Likar, and F. Pernuš, "A review of 3D/2D registration methods for image-guided interventions," *Medical image analysis* **16,** 642–661 (2012).

[167] Y. Nakajima, T. Tashiro, N. Sugano, K. Yonenobu, T. Koyama, Y. Maeda, Y. Tamura, M. Saito, S. Tamura, M. Mitsuishi, N. Sugita, I. Sakuma, T. Ochi, and Y. Matsumoto, "Fluoroscopic bone fragment tracking for surgical navigation in femur fracture reduction by incorporating optical tracking of hip joint rotation center," *IEEE transactions on bio-medical engineering* **54,** 1703–1706 (2007).

[168] B. Jaramaz and K. Eckman, "2D/3D Registration for Measurement of Implant Alignment After Total Hip Replacement," *Medical Image Computing and Computer-Assisted Intervention - MICCAI 2006, Lecture Notes in Computer Science* **4191,** 653–661 (2006).

[169] D. Knaan and L. Joskowicz, "Effective Intensity-Based 2D / 3D Rigid Registration between Fluoroscopic X-Ray and CT," in *Medical image computing and computer-assisted intervention - MICCAI International Conference on Medical Image Computing and Computer-Assisted Intervention* (2003), pp. 351–358.

[170] M. R. Mayberg, E. LaPresto, and E. J. Cunningham, "Image-guided endoscopy: description of technique and potential applications," *Neurosurgical Focus* **19,** 1–5 (2005).

[171] T. M. Peters, "Image-guidance for surgical procedures," *Physics in medicine and biology* **51,** R505–R540 (2006).

[172] L. Caponetti and A. Fanelli, "3D Bone reconstruction from two X-Ray views," *Annual International Conference of the IEEE Engineering in Medicine and Biology Society* **12,** 208–210 (1990).

[173] a. Le Bras, S. Laporte, V. Bousson, D. Mitton, J. De Guise, J. Laredo, and W. Skalli, "Personalised 3D reconstruction of proximal femur from low-dose digital biplanar radiographs," *International Congress Series* **1256,** 214–219 (2003).

[174] a. Le Bras, S. Laporte, D. Mitton, J. a. de Guise, and W. Skalli, "Three-dimensional (3D) detailed reconstruction of human vertebrae from low-dose digital stereoradiography," *European Journal of Orthopaedic Surgery & Traumatology* **13,** 57–62 (2003).

[175] S. Laporte, W. Skalli, J. a. de Guise, F. Lavaste, and D. Mitton, "A biplanar reconstruction method based on 2D and 3D contours: application to the distal femur," *Computer methods in biomechanics and biomedical engineering* **6,** 1–6 (2003).

[176] A. Baudoin, W. Skalli, J. a. de Guise, and D. Mitton, "Parametric subject-specific model for in vivo 3D reconstruction using bi-planar X-rays: application to the upper femoral extremity," *Medical and biological engineering and computing* **46,** 799–805 (2008).

[177] R. Kurazume, K. Nakamura, T. Okada, Y. Sato, N. Sugano, T. Koyama, Y. Iwashita, and T. Hasegawa, "3D reconstruction of a femoral shape using a parametric model and two 2D fluoroscopic images," *Computer Vision and Image Understanding* **113,** 202–211 (2009).

[178] R. Kurazume, K. Nakamura, T. Okada, Y. Sato, N. Sugano, T. Koyama, Y. Iwashita, and T. Hasegawa, "3D reconstruction of a femoral shape using a parametric model and two 2D fluoroscopic images," *Computer Vision and Image Understanding* **113,** 202–211 (2009).

[179] G. Zheng, S. Gollmer, S. Schumann, X. Dong, T. Feilkas, and M. a. González Ballester, "A 2D/3D correspondence building method for reconstruction of a patient-specific 3D bone surface model using point distribution models and calibrated X-ray images," *Medical image analysis* **13,** 883–899 (2009).

[180] M. Fleute, S. Lavallée, and L. Desbat, "Integrated approach for matching statistical shape models with intra-operative 2D and 3D data," *Medical Image Computing and Computer-Assisted Intervention* 364–372 (2002).

[181] O. Ahmad, K. Ramamurthi, K. E. Wilson, K. Engelke, R. L. Prince, and R. H. Taylor, "Volumetric DXA (VXA): A new method to extract 3D information from multiple in vivo DXA images," *Journal of bone and mineral research* **25,** 2744–2751 (2010).

[182] T. Whitmarsh, L. Humbert, M. De Craene, L. M. Del Rio Barquero, and A. F. Frangi, "Reconstructing the 3D Shape and Bone Mineral Density Distribution of the Proximal Femur from Dual-energy X-ray Absorptiometry," *IEEE transactions on medical imaging* **30,** 2101–2114 (2011).

[183] L. Humbert, T. Whitmarsh, M. D. Craene, L. M. Del Río Barquero, and A. F. Frangi, "Technical note: comparison between single and multiview simulated DXA configurations for reconstructing the 3D shape and bone mineral density distribution of the proximal femur," *Medical physics* **39,** 5272–5276 (2012).

[184] A. Hurvitz and L. Joskowicz, "Registration of a CT-like atlas to fluoroscopic X-ray images using intensity correspondences," *International Journal of Computer Assisted Radiology and Surgery* **3,** 493–504 (2008).

[185] R. Bryan, P. B. Nair, and M. Taylor, "Use of a statistical model of the whole femur in a large scale, multi-model study of femoral neck fracture risk," *Journal of biomechanics* **42,** 2171–2176 (2009).

[186] O. M. Ahmad, K. Ramamurthi, K. E. Wilson, K. Engelke, M. Bouxsein, and R. H. Taylor, "3D structural measurements of the proximal femur from 2D DXA images using a statistical atlas," in *SPIE Medical Imaging* (2009), pp. 726005–4 – 726005–8.

[187] J. Yao and R. Taylor, "A multiple-layer flexible mesh template matching method for non-rigid registration between a pelvis model and CT images," in *Proc. SPIE 5032, Medical Imaging 2003: Image Processing, 1117* (2003).

[188] T. Whitmarsh, L. Humbert, L. M. del Rio Barquero, S. Di Gregorio, A. F. Frangi, and L. M. Del Río Barquero, "3D reconstruction of the lumbar vertebrae from anteroposterior and lateral dual-energy X-ray absorptiometry," *Medical image analysis* **17,** 475–487 (2013).

[189] G. J. Tornai, G. Cserey, and I. Pappas, "Fast DRR generation for 2D to 3D registration on GPUs," *Medical physics* **39,** 4795–4799 (2012).

[190] J. Yao and R. Taylor, "Assessing accuracy factors in deformable 2D/3D medical image registration using a statistical pelvis model," in *Proceedings of the Ninth IEEE International Conference on Computer Vision* (2003), pp. 1329–1334.

[191] T. S. Y. Tang and R. E. Ellis, "2D/3D deformable registration using a hybrid atlas.," in *Medical image computing and computer-assisted intervention-MICCAI International Conference on Medical Image Computing and Computer-Assisted Intervention* (2005), pp. 223–230.

[192] T. Rikkonen, K. Salovaara, J. Sirola, M. Kärkkäinen, M. Tuppurainen, J. Jurvelin, R. Honkanen, E. Alhava, and H. Kröger, "Physical activity slows femoral bone loss but promotes wrist fractures in postmenopausal women: a 15-year follow-up of the OSTPRE study," *Journal of bone and mineral research* **25,** 2332–2340 (2010).

[193] M. Tuppurainen, H. Kröger, S. Saarikoski, R. Honkanen, and E. Alhava, "The effect of previous oral contraceptive use on bone mineral density in perimenopausal women," *Osteoporosis international* **4,** 93–98 (1994).

[194] Q. Fang and D. A. Boas, "Tetrahedral mesh generation from volumetric binary and grayscale images," in *2009 IEEE International Symposium on Biomedical Imaging: From Nano to Macro* (2009), pp. 1142–1145.

[195] M. Viceconti, F. Taddei, L. Montanari, D. Testi, A. Leardini, G. Clapworthy, and S. Van Sint Jan, "Multimod Data Manager: a tool for data fusion," *Computer methods and programs in biomedicine* **87,** 148–159 (2007).

[196] G. Bergmann, G. Deuretzbacher, M. Heller, F. Graichen, A. Rohlmann, J. Strauss, and G. N. Duda, "Hip contact forces and gait patterns from routine activities," *Journal of biomechanics* **34,** 859–871 (2001).

[197] L. Grassi, N. Hraiech, E. Schileo, M. Ansaloni, M. Rochette, and M. Viceconti, "Evaluation of the generality and accuracy of a new mesh morphing procedure for the human femur.," *Medical engineering & physics* **33,** 112–20 (2011).

[198] T. Whitmarsh, L. Humbert, M. De Craene, L. M. del Río Barquero, K. Fritscher, R. Schubert, F. Eckstein, T. Link, and A. F. Frangi, "3D Bone Mineral Density Distribution and Shape Reconstruction of the Proximal Femur from a Single Simulated DXA Image: An In Vitro Study," in *Proceedings of SPIE Medical Imaging 2010: Image Processing*, Vol. 7623 (2010), p. 76234U.

[199] P. A. Toogood, A. Skalak, and D. R. Cooperman, "Proximal femoral anatomy in the normal human population," *Clinical orthopaedics and related research* **467,** 876–885 (2009).

[200] C. M. Langton, S. Pisharody, and J. H. Keyak, "Comparison of 3D finite element analysis derived stiffness and BMD to determine the failure load of the excised proximal femur," *Medical engineering and physics* **31,** 668–672 (2009).

[201] J. H. Waarsing, R. M. Rozendaal, J. A. N. Verhaar, S. M. A. Bierma-Zeinstra, and H. Weinans, "A statistical model of shape and density of the proximal femur in relation to radiological and clinical OA of the hip," *Osteoarthritis and cartilage* **18,** 787–794 (2010).

[202] R. L. Jaarsma, N. Verdonschot, R. van der Venne, and A. van Kampen, "Avoiding rotational malalignment after fractures of the femur by using the profile of the lesser trochanter: an in vitro study," *Archives of orthopaedic and trauma surgery* **125,** 184–187 (2005).

[203] J. H. Keyak, S. A. Rossi, K. A. Jones, C. M. Les, and H. B. Skinner, "Prediction of fracture location in the proximal femur using finite element models.," *Medical engineering and physics* **23,** 657–64 (2001).

[204] J. H. Keyak, S. A. Rossi, K. A. Jones, and H. B. Skinner, "Prediction of femoral fracture load using automated finite element modeling," *Journal of biomechanics* **31,** 125–133 (1998).

[205] C. Perry, "Strain-Gage Reinforcement Effects on Orthotropic Materials," in *Manual on Experimental Methods for Mechanical Testing of Composites* (Springer Netherlands, 1989), pp. 39–44.

[206] J. H. Keyak, "Improved prediction of proximal femoral fracture load using nonlinear finite element models," *Medical engineering and physics* **23,** 165–173 (2001).

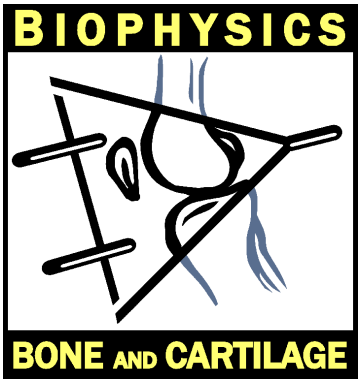

Sami Väänänen

Functional Imaging of Proximal Femur by Combining Dual Energy X-ray Imaging and Finite Element Simulations

Over 200 million people worldwide suffer from osteoporosis. Osteoporosis is currently diagnosed based on the bone mineral density (BMD) of the femur or lumbar spine measured with dual-energy X-ray absorptiometry (DXA). However, the BMD measured with two-dimensional DXA is only a moderate predictor of fracture risk. In this thesis, novel image analysis and mechanical simulation methods are presented which enable automatic estimation of the three-dimensional shape and morphology of the femur, as well as the femoral fracture strength from single DXA image. The developed methodology may improve the fracture risk prediction of the femur and the diagnostics of osteoporosis in the future.

UNIVERSITY OF
EASTERN FINLAND

Publications of the University of Eastern Finland
Dissertations in Forestry and Natural Sciences

ISBN 978-952-61-1536-8